STP 1597, 2018 / available online at www.astm.org / doi: 10.1520/STP159720160055

Adrien Couet,[1] Arthur T. Motta,[2] Antoine Ambard,[3] and
Robert J. Comstock[4]

Hydrogen Pickup Mechanism in Zirconium Alloys

Citation

Couet, A., Motta, A. T., Ambard, A., and Comstock, R. J., "Hydrogen Pickup Mechanism in Zirconium Alloys," *Zirconium in the Nuclear Industry: 18th International Symposium, ASTM STP1597*, R. J. Comstock and A. T. Motta, Eds., ASTM International, West Conshohocken, PA, 2018, pp. 312–349, http://dx.doi.org/10.1520/STP159720160055[5]

ABSTRACT

Because hydrogen ingress into zirconium cladding can cause embrittlement and limit cladding lifetime, hydrogen pickup during corrosion is a critical life-limiting degradation mechanism for nuclear fuel. However, mechanistic knowledge of the oxidation and hydrogen pickup mechanisms is still lacking. In an effort to develop such knowledge, we conducted a comprehensive study that included detailed experiments combined with oxidation modeling. We review this set of results conducted on zirconium alloys herein and articulate them into a unified corrosion theoretical framework. First, the hydrogen pickup fraction (f_H) was accurately measured for a specific set of alloys specially designed to determine the effects of alloying elements, microstructure, and corrosion kinetics on f_H. We observed that f_H was not constant and increased until the kinetic transition and decreased at the transition. f_H depended on the alloy and was lower for niobium-containing alloys. These results led us to hypothesize that hydrogen pickup during corrosion results from the need to balance the charge during the corrosion reaction such that f_H decreases when the rate of electron transport through the protective oxide increases. To assess this hypothesis, two experiments were performed: (1) micro-X-ray absorption

---

Manuscript received March 1, 2016; accepted for publication July 28, 2016.

[1] University of Wisconsin–Madison, Dept. of Engineering Physics, 1500 Engineering Dr., Madison, WI 53706

[2] Pennsylvania State University, Dept. of Mechanical and Nuclear Engineering, University Park, PA 16802

[3] EDF R&D, Materials and Mechanics of Components, Ecuelles, 77818 Moret-sur-Loing, France

[4] Westinghouse Electric Company, 1332 Beulah Rd., Pittsburgh, PA 15235

[5] ASTM 18th International Symposium on *Zirconium in the Nuclear Industry* on May 15-19, 2016 in Hilton Head, SC.

near-edge spectroscopy (μ-XANES) to investigate the evolution of the oxidation state of alloying elements when incorporated in the growing oxide and (2) in situ electrochemical impedance spectroscopy (EIS) to measure oxide resistivity as a function of exposure time on different alloys. With the use of these results, we developed an analytical zirconium alloy corrosion model based on the coupling of oxygen vacancies and electron currents. Both modeling and EIS results show that as the oxide electric conductivity decreases the f_H increases. These new results support the general hypothesis of charge balance. The model quantitatively and qualitatively predicts the differences observed in oxidation kinetics and hydrogen pickup fraction between different alloys.

Keywords

hydrogen pickup, zirconium corrosion, oxidation model, XANES, EIS

Introduction

Hydrogen absorption into fuel cladding can cause embrittlement and limit cladding lifetime. Consequently, hydrogen pickup during corrosion is a critical life-limiting degradation mechanism for nuclear fuel. This is especially true for the higher fuel duties currently used in the industry. However, mechanistic knowledge of the hydrogen pickup mechanism is incomplete [1,2]. Although it is understood that different alloys exhibit not only different corrosion kinetics but also different hydrogen pickup rates at a given stage of corrosion [3–6], a complete understanding of the role of alloying elements in the corrosion and hydrogen pickup mechanisms is still lacking. The corrosion performance of zirconium (Zr) alloys worsens as the alloy purity increases, and almost any alloying addition (even at very small proportions) increases corrosion resistance [7]. On the other hand, these additions can have dramatic effects on hydrogen pickup, with niobium additions usually resulting in a significant reduction in hydrogen pickup [8] and nickel additions increasing hydrogen pickup [9].

The overall corrosion reaction (Eq 1) is:

$$\mathrm{Zr} + 2\mathrm{H_2O} \rightarrow \mathrm{ZrO_2} + 2\mathrm{H_2} \quad (1)$$

However, not all the hydrogen evolves as H_2, and a significant amount can be absorbed by the Zr metal and form hydrides, which embrittle the fuel cladding. It is now accepted that the hydrogen absorbed into the cladding comes from the corrosion reaction and that the amount depends on the corrosion rate [10,11]. The corrosion rate of Zr alloys in the protective regime can usually be described by a power law [12] (see **Table A1** for a list of all parameters and variables and their definitions):

$$\delta(t) = kt^n \quad (2)$$

This protective regime persists until the oxide transition, which is defined as the stage in the corrosion process at which a sudden increase in corrosion rate occurs ($\delta = \sim 2\text{–}3\ \mu\text{m}$). Careful analysis by power law fitting of the pretransition oxidation kinetics obtained experimentally on Zr alloys has shown a wide range of values of n, which are characteristic of each alloy. It is important to note that the value of n is often related to the alloy composition, such that zirconium-niobium (Zr-Nb) alloys generally exhibit close to parabolic oxidation kinetics [5,8], whereas Zircaloys and more generally precipitate-forming alloys exhibit kinetics closer to cubic or even sub-cubic ($n \leq 0.3$) [6,13–15]. Although the parameter n in these fits is not easily derivable from existing theories of metal oxidation, its reproducibility is a clear phenomenological evidence of a consistent mechanistic deviation from the oxidation mechanism derived by Wagner and Schottky [16] and Hauffe [17], which predicts parabolic growth of thick oxides. Considering the differences in pretransition oxidation kinetics between alloys, multiple theories have been derived to explain the observed deviation from parabolic oxidation kinetics, the more interesting being based on the evolution of oxide stresses [18], oxide space charge [19,20], and the development of oxide cracks [6]. The post-transition regime of Zircaloy-4 and Zr-Nb alloys can be divided into several periods of corrosion that cyclically reproduce the pretransition regime [21,22].

Every attempt to model Zr corrosion mechanism struggles with the difficulty of combining both the oxidation and hydrogen pickup kinetics into a single corrosion model. The purpose of this paper was to propose a unified corrosion model that accounts both for the experimentally observed oxidation and hydrogen pickup kinetics. Multiple consistent and precise measurements (weight gain and hydrogen content) are presented for a specific set of alloys exposed to pure 360°C water in an autoclave to clearly present how alloying elements affect oxidation kinetics and the hydrogen pickup fraction in this environment. We mainly focus on niobium and iron alloying additions, whereas the other alloying elements such as chromium and tin in Zircaloy-4 are not covered in detail. From these basic experimental observations, two research objectives are detailed. The first is to explain the significant effect of alloying additions on oxidation kinetics. The second is to explain the differences in the hydrogen pickup fraction between different alloys and to relate these differences to the differences in oxidation kinetics. The oxide transition phenomenon is not covered in this paper because it is believed that the occurrence of the transition depends on the evolution of oxide stresses, which are not considered herein. From these motivations, a general hypothesis of the proposed model is detailed. Specific state-of-the-art experiments (X-ray absorption near-edge spectroscopy [XANES] and in situ electrochemical impedance spectroscopy [EIS]) were performed to validate the hypothesis. A corrosion model was then derived analytically for the specific case of electroneutral oxides that fits Zr-Nb oxidation kinetics.

In addition, the theory was developed for a more general case, including oxide space-charge effects. In light of the experiments and the model results, a hydrogen pickup theory is finally developed.

Autoclave Corrosion Experiments

ZIRCONIUM ALLOYS STUDIED

In this study, various alloys were tested: three Zr-Nb alloys (Zr-0.4Nb, heat-treated Zr-1.0Nb, and Zr-2.5Nb) and two Zircaloy-4 materials. These alloy samples were corroded in stainless steel autoclaves in 360°C pure water at saturation pressure (18 MPa). Hydrogen evolved from the oxidation process was limited to a maximum of 40 cc/kg(H_2O) by periodically opening the autoclave for interim weight gain measurements. Thus, the hydrogen concentration did not increase significantly in the autoclave during the corrosion experiments. The samples included both sheet coupons (Zr-0.4Nb, Zr-1.0Nb, and Zircaloy-4) and tubing (Zr-2.5Nb and Zircaloy-4). The tube samples were designed for in situ EIS experiments, as detailed later, whereas the Zr-Nb sheet samples were model alloys. Multiple Zr-Nb alloys were chosen to compare the effect of niobium in solid solution (in α-Zr for Zr-0.4Nb and in both α- and β-Zr for heat-treated Zr-1.0Nb as discussed later) with the effect of niobium in β-niobium precipitates (in Zr-2.5Nb alloys).

The manufacturing process of the tubes has been detailed previously [3]. Sheet fabrication consisted of β-quenching followed by hot rolling to an intermediate thickness. After conditioning the hot-rolled plate, multiple iterations of cold rolling and recrystallization annealing in the single-phase temperature range reduced the sheet to a final thickness. The final annealing temperature, which was less than 600°C for Zr-Nb alloys and less than 700°C for Zircaloy-4, resulted in a fully recrystallized microstructure. According to the phase diagram, it is expected that niobium atoms will be in solid solution in the Zr-0.4Nb sheet [23]. The Zr-1.0Nb sheet was subsequently annealed at 720°C (two-phase temperature range) for 24 h to intentionally alter the niobium distribution. Rather than having β-niobium particles in the α-Zr matrix, the alloy exhibited α-Zr grains with β-Zr present on the grain boundaries. It is expected that the β-niobium particles in α-Zr would have dissolved during the two-phase annealing treatment and that the supersaturated niobium diffused to the β-Zr phase, leaving a niobium-saturated α-Zr phase. Detailed transmission electron microscopy (TEM) microstructure characterizations of the heat-treated Zr-1.0Nb alloy can be found in Hu et al. [24], whereas the other alloy microstructure characterizations can be found in Couet, Motta, and Comstock [3] and Couet, Motta, and Ambard [20].

OXIDATION KINETICS

The oxidation kinetics for Zircaloy-4 and heat-treated Zr-1.0Nb sheet coupons are plotted in **Fig. 1**. The equivalent data for the Zr-0.4Nb, Zr-2.5Nb, and Zircaloy-4 tube alloys are available in Couet, Motta, and Comstock [3] and Couet, Motta, and Ambard [20] and are reproduced in **Fig. 2** for the ease of understanding. The pre- and first-transition regimes were fitted to a power law in the form of Eq 2. There was excellent agreement between the power law fits and experimental data (each data point represents the average weight gain of all sister samples—typically ten, except for only two samples of Zr-0.4Nb—and the error bars—almost invisible at this scale—correspond to the standard deviations among the samples). The trends discussed previously were clearly confirmed by the following data:

- In **Fig. 1**, the heat-treated Zr-1.0Nb alloy shows close to parabolic oxidation kinetics, whereas Zircaloy-4 shows sub-cubic kinetics. Almost perfect parabolic kinetics have also been observed for the Zr-0.4Nb alloy (see **Fig. 2**), although longer exposure times for this alloy could not be achieved because of the lack of coupons. On the other hand, Zr-2.5Nb oxidation kinetics are clearly sub-parabolic ($n = 0.37$).
- The oxidation kinetics of Zircaloy-4 sheet and tube are mostly sub-cubic ($n = \sim 0.29$) and are very similar to each other.

FIG. 1 Oxidation kinetics of Zircaloy-4 and Zr-1.0Nb sheet coupons. The power law fits and their equations are also shown.

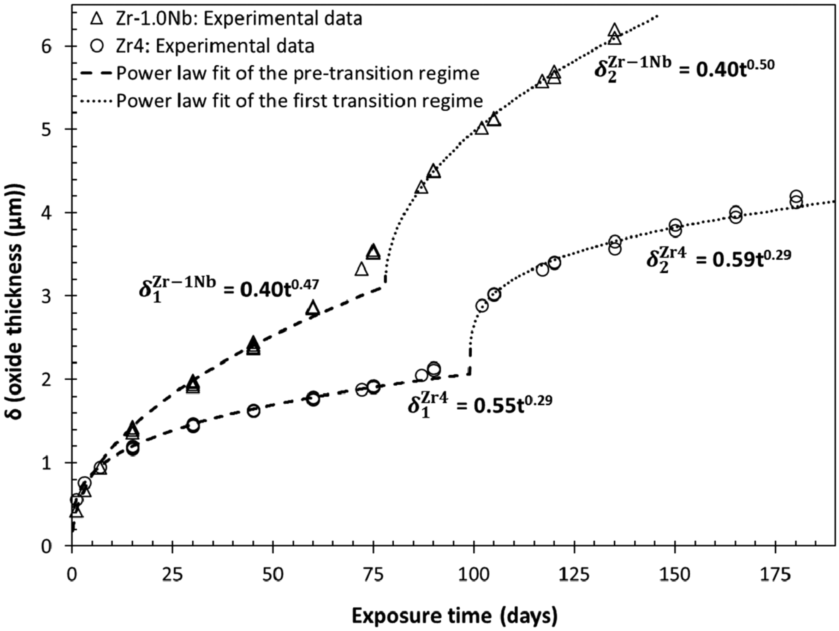

FIG. 2 Oxidation kinetics of the Zircaloy-4 tube, Zr-2.5Nb tube, and Zr-0.4Nb sheet coupons. The power law fits and their equations are also shown.

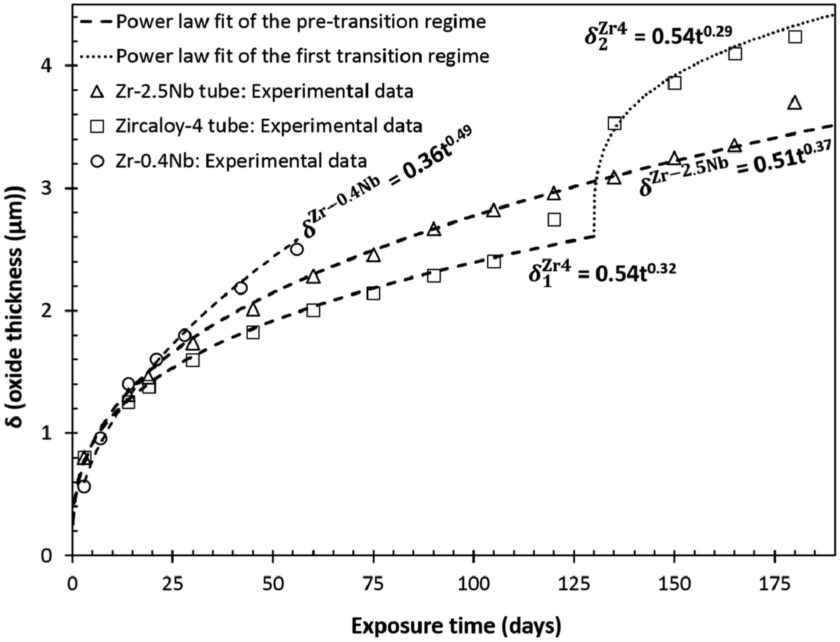

- For all alloys, the oxidation kinetics and their power law fits are essentially identical in the pre- and post-transition regimes, suggesting that the corrosion mechanism does not depend on the regimes considered.
- The transition time and oxide thickness are also different between the alloys.

As detailed in the Introduction, one of the objectives of this study was to rationalize the significant effect of niobium and iron alloying additions on oxidation kinetics.

TOTAL HYDROGEN PICKUP FRACTION

In order to compare the hydrogen pickup of different alloys, it is necessary to quantify the amount of hydrogen picked up relative to the amount of corrosion. To this end, the hydrogen content in the metal is measured and normalized to the total hydrogen generated in the corrosion reaction during exposure [3]. As discussed previously, only the hydrogen generated by the corrosion reaction is susceptible to entering the metal [25]. Thus, the total hydrogen pickup fraction, f_H^t, is defined as the ratio of the hydrogen absorbed to the total amount of hydrogen generated by the corrosion reaction from the beginning of the corrosion test up to time t (Eq 3):

$$f_H^t = \frac{\Delta_0^t H_{absorbed}}{\Delta_0^t H_{generated}} \tag{3}$$

Fig. 3 plots the hydrogen content versus weight gain normalized to the sample area for both heat-treated Zr-1.0Nb and Zircaloy-4 alloys (data regarding the other alloys can be found in Couet, Motta, and Comstock. [3]). The dotted lines showing the constant hydrogen pickup fraction f_H^t are also indicated. This representation allows for an easy comparison of the hydrogen pickup kinetics of alloys with different oxidation kinetics.

It is clearly observed in Fig. 3 that f_H^t (Zircaloy-4) is greater than f_H^t (Zr-1.0Nb) at any stage of corrosion, confirming the beneficial effect of niobium on hydrogen pickup fraction compared with that of other alloying elements in Zircaloy-4 (tin, iron, chromium). Even though this beneficial effect has been known for a long time and has been the basis for the development of new alloys in the industry [26,27], so far no satisfactory detailed mechanism has been developed to explain this behavior. Thus, as mentioned in the Introduction, another motivation of this paper was to understand the beneficial effect of niobium on f_H^t compared with other alloying elements such as iron (chromium and tin were not as deeply covered in this study) and to relate this effect to the differences in oxidation kinetics observed in Fig. 1 and Fig. 2.

INSTANTANEOUS HYDROGEN PICKUP FRACTION

It is observed in Fig. 3 that f_H^t was not constant but increased throughout corrosion and from one transition regime to the next. It is also observed that f_H^t increased significantly before transition and appears to have been stable at transition. These trends have been observed before [28,29] and are best characterized by computing

FIG. 3 Hydrogen content as function of weight gain and oxide thickness. The dotted lines correspond to constant values of f_H^t.

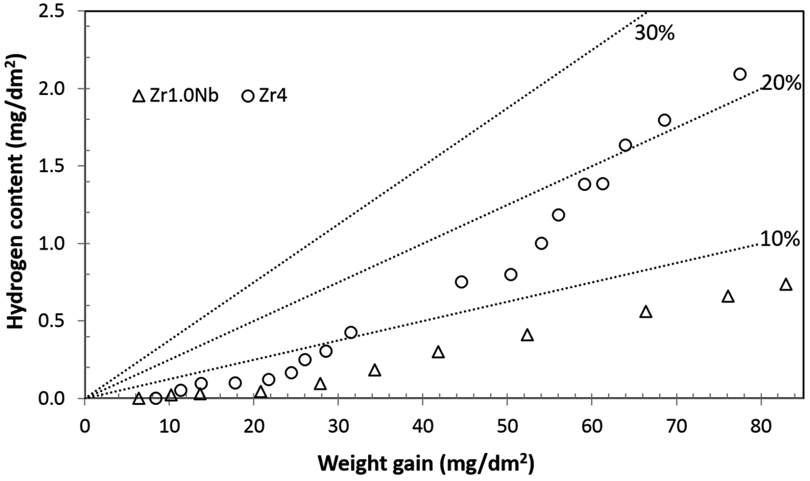

the instantaneous hydrogen pickup fraction f_H^i. The instantaneous hydrogen pickup fraction f_H^i is defined as the ratio of the hydrogen absorbed between time t and time $t + \Delta t$ to the total amount of hydrogen generated by the corrosion reaction during the same time interval. The f_H^i for both heat-treated Zr-1.0Nb and Zircaloy-4 sheet alloys are plotted in Fig. 4 and Fig. 5, respectively, along with the corresponding oxidation kinetics already detailed in Fig. 1.

Both alloys exhibited the now well-known periodic behavior of the instantaneous hydrogen pickup fraction (Zr-2.5Nb and Zircaloy-4 tubes show similar periodic behavior [3]). Basically, f_H^i increases significantly before transition and decreases at transition, its periodic behavior following the periodicity of oxidation kinetics. Of course, the magnitude of the f_H^i for both alloys are quite different (which is why the f_H^t are different for both alloys), but the underlying mechanism is nevertheless the same. Thus, the last motivation of the paper was to explain the periodic behavior of f_H^i in all alloys and to relate it to the corrosion kinetics and hydrogen pickup observed previously.

The general hypothesis of the proposed model based on alloying solute additions, which can simultaneously explain the behavior of oxidation kinetics as well as the f_H^t and f_H^i of different alloys, is detailed in the following section. It should be noted that the proposed model only covers Zr alloys that show protective oxidation behavior in pure water autoclaves under nonirradiating conditions.

FIG. 4 Instantaneous hydrogen pickup fraction as function of exposure time for Zr-1.0Nb. The oxidation kinetics are also plotted.

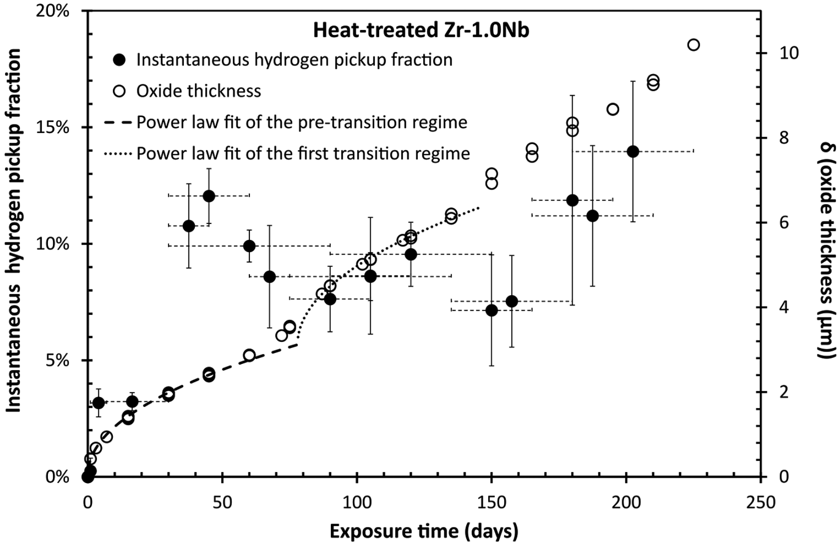

FIG. 5 Instantaneous hydrogen pickup fraction as function of exposure time for Zircaloy-4. The oxidation kinetics are also plotted.

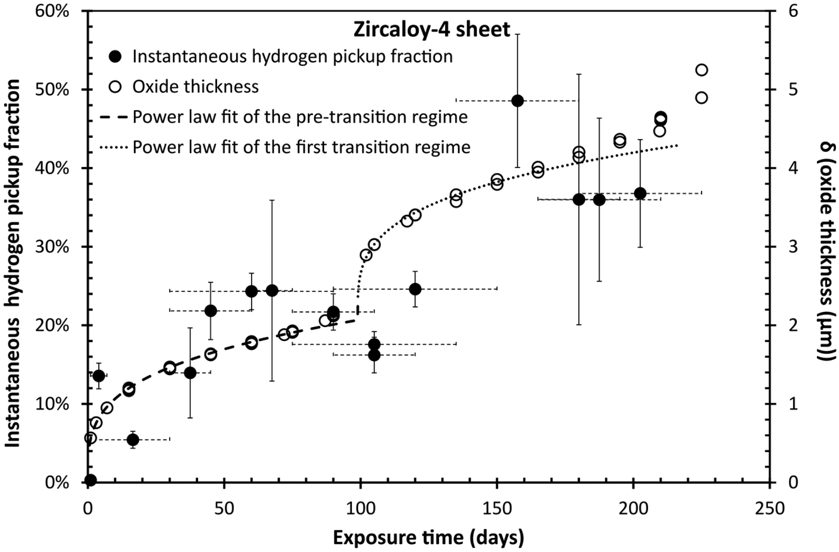

General Hypothesis

The results presented in Figs. 1–5 indicate an empirical inverse relation between the hydrogen pickup fraction and the oxidation kinetics: the higher the n, the lower the f_H^t, and vice versa. Because this trend has been consistently observed, it is critical that a proposed first-principle Zr corrosion model reproduce it.

Because hydrogen is part of the corrosion process, it is natural to assume that its absorption and transport is one part of the cathodic reaction of the corrosion mechanism—the other part being the transport of electrons to the oxide-water interface (see Motta, Couet, and Comstock [1] for a detailed description of the corrosion reaction steps). Under the experimental conditions considered, the corrosion mechanism of Zr alloys is limited by the transport of charged species across the protective oxide layer, so that the corrosion rate depends on the resistance of the protective oxide layer to these respective transports (namely the migration of oxygen vacancies, electrons, and protons). The general hypothesis to rationalize the observed hydrogen pickup is to consider that if the oxide resistivity is high, electron transport is slow, which increases the driving force for proton absorption at the oxide-water interface. Basically, hydrogen pickup increases when electron transport becomes more difficult, requiring hydrogen ingress to close the cathodic reaction. Thus, the electronic resistivity of the protective oxide is a key parameter in controlling the oxidation kinetics and hydrogen pickup, as has previously been suggested [30–32].

Fig. 6 is a schematic presenting the hydrogen pickup mechanism hypothesis. In this case, it is supposed that oxygen vacancy transport through the oxide is more difficult than electron transport. Indeed, in that case, the electric field at the metal-oxide interface will be positive to repel the slowest species (in this case the oxygen vacancy), and thus the electric potential across the oxide will be negative ($\Delta V_{\text{ox}} < 0$).

This potential gradient aims at increasing (respectively reducing) the flux of the oxygen vacancies (respectively electrons). A low (respectively high) oxide electronic resistivity will result in a low (respectively high) oxide electric potential, which in turn will increase (respectively decrease) the interfacial potential at the oxide-water interface. Indeed, the corrosion potential (given by $V_{\text{W/O}} - V_{(\text{M/O})}$) is fixed because the system boundaries are supposed to be at thermodynamic equilibrium. However, the repartition of the potential in the system can vary between the interfacial drops and the potential in the oxide, as indicated by the dotted curves in Fig. 6. That is why a higher oxide resistivity will reduce the interfacial drop at the oxide-water interface, reducing the activation energy for proton absorption. In summary, a high (resp. low) oxide electronic resistivity will increase (resp. reduce) the driving force for hydrogen absorption. In other words, if electrons cannot close the reaction, the driving force to close it with hydrogen increases.

The effect of alloying elements in this proposed mechanism is as follows. It is emphasized that corrosion is an equilibrium process under significant constraints,

FIG. 6 Schematic of the general hydrogen pickup mechanism hypothesis based on oxide electronic conductivity. $V_{\text{M/O}}$ and $V_{\text{W/O}}$ are fixed potentials at the boundaries, and the arrows represent the electron and vacancy currents.

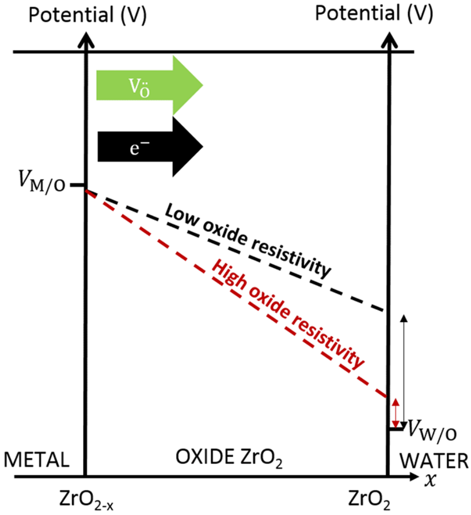

such that the effects of alloying elements in oxide solid solution differ considerably from those observed in a classic semiconductor-doping effect under thermodynamic equilibrium conditions. Indeed, in the case of a semiconductor, the doping effects on material transport properties depend on the differences in the number of valence electrons between the dopant and semiconductor material considered [33,34]. However, in the case of corrosion, the oxide is under significant dynamic constraints because an electric potential is "applied" on its sides and charged species diffuse through its lattice. These conditions result in a nonsteady-state reorganization of charges across the bulk oxide (namely oxide space charges), the magnitude of which depends significantly on the oxide properties (the dielectric constant and relevant diffusion parameters) and the corrosion potential that sets the boundary conditions [35,36].

In situations of oxide growth by charged particle transport, there can be no question as to whether there is space charge in the oxide because the mobile-charged particles themselves constitute space charge. The only question is whether the level of the space charge is sufficiently high to modify the oxide electric potential. Clearly, in addition to the mobile-charged particles, the oxidized alloying elements in oxide solid solution will either reduce or increase space-charge effects depending on their stable oxidation state. It is thus much more difficult to qualitatively predict the effects of alloying elements during corrosion processes than it is in the doping of semiconductors.

This paper helps to predict the effects of alloying elements on Zr alloy corrosion by introducing the concept of space-charge compensation. It is proposed that the alloying elements present in protective Zr-oxide layers act by compensating (i.e., reducing) the oxide space charge due to diffusing species, their compensation effect depending on their oxidation states and concentrations in oxide solid solution. This compensation effect will reduce the apparent oxide resistivity that, according to **Fig. 6**, will in turn increase the activation energy for proton absorption, reducing the hydrogen pickup fraction.

It is proposed that niobium and iron in oxide solid solution compensate oxide space charges. To compensate the positive oxide space charges, the oxidation state of iron and niobium must be lower than 4+. Because the niobium solubility limit in the metal is at least one order of magnitude higher than that of iron or chromium [37], the niobium effect would be more significant than that of iron and chromium in space-charge compensation. (Tin is not considered because its oxidation state is not well defined [38–40] and could be mainly 4+, in which case it would not affect space charge.)

The general corrosion mechanism and alloying element effect hypotheses were tested experimentally and are presented in the next section. To verify whether there is indeed enough oxidized niobium or iron in solid solution with an oxidation state below 4+ to compensate space charges, we performed μ-XANES experiments on Zr-0.4Nb and Zircaloy-4 alloys. EIS experiments were then performed to measure and compare the apparent oxide resistivity $\rho_{ZrO_2}^{EIS}$ in Zircaloy-4 and Zr-2.5Nb tube alloys at different stages of corrosion as well to verify whether $\rho_{ZrO_2}^{EIS}$ and f_H^i variations are correlated. A first-principle model based on these results was then extensively developed to qualitatively and quantitatively explain the experimental observations.

Experimental Methods and Results

XANES EXPERIMENTS

μ-XANES experiments were performed at the 2ID-D beamline of the Advanced Photon Source (APS) at Argonne National Laboratory. Details on this experiment can be found in Couet et al. [41]. Pretransition Zr-0.4Nb ($\delta = \sim 2.5$ μm) and Zircaloy-4 ($\delta = \sim 1.3$ μm) oxides were prepared in the form of small transverse cross-sections. The X-ray microprobe in the experimental station produces a monochromatic X-ray beam of size 0.2 by 0.2 μm (full width at half maximum), which allows to precisely probe different locations in the oxide at various distances from the oxide-metal interface. XANES signals were acquired and fitted to niobium and iron standards with different oxidation states so that the percentages of oxidized niobium and iron at different locations in the oxide were determined [41]. The niobium K-edge XANES signal in the case of Zr-0.4Nb comes entirely from niobium in solid solution, whereas in the case of Zircaloy-4, the iron K-edge XANES signal is a convolution between iron in precipitates and in solid solution. However, a special sample preparation, detailed in Couet et al. [41], allowed to only probe the iron in solid solution in the oxide. The results are plotted in Fig. 7 for the two alloys. The total amounts of oxidized niobium and iron (in wt.%) in solid solution determined by XANES are plotted as black points as functions of the normalized pretransition oxide depth. The linear dashed lines correspond to the theoretical total amount of niobium and iron available in oxide solid solution in these alloys (assuming, for

FIG. 7 XANES results on solid-solution niobium in Zr-0.4Nb and solid-solution iron in Zircaloy-4. Theoretical amounts of niobium and iron in the oxide (assuming same solubility as in the metal) are shown as dashed lines.

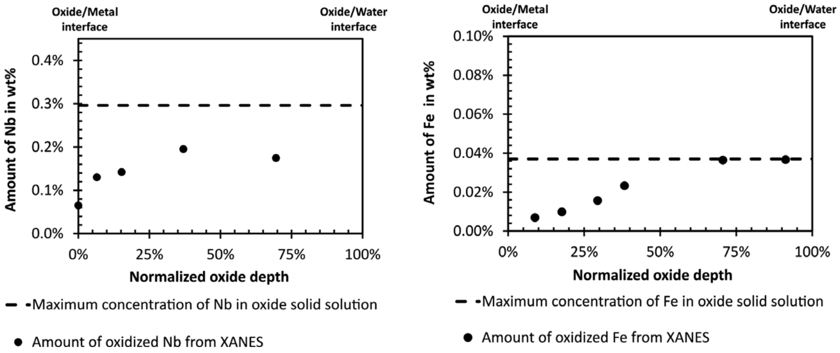

lack of available data, that the solubility limits of both metal and oxide are identical): 0.4 wt.% for niobium in Zr-0.4Nb (i.e., 0.3 wt.% Zr oxide) and 0.05 wt.% for iron in Zircaloy-4 (i.e., 0.04 wt.% Zr oxide) [37,42–44].

Starting with the Zr-0.4Nb alloy, the results show that the niobium oxidation was delayed compared with the Zr matrix such that metallic niobium in solid solution was embedded in the oxide. An analysis of the XANES spectra showed that niobium oxidation states in Zr-0.4Nb oxides were mostly 2+ and 3+, whereas 5+ was only observed very close to the oxide-water interface [20,41,45–47]. The fraction of oxidized niobium increased as the distance to the oxide-metal interface increased, reaching approximately two-thirds halfway through the oxide.

Similar to the niobium in Zr-Nb alloys, an analysis of the XANES spectra for the Zircaloy-4 sample showed that the iron oxidation was delayed compared with the Zr matrix such that metallic iron in solid solution was embedded in the oxide. An analysis of the XANES spectra showed that the oxidation states of iron in the oxide were 2+ and 3+.

Although there is undoubtedly oxidized niobium and iron in oxide solid solution with an oxidation state lower than 4+, resulting in oxide space-charge compensation, it is not known whether these oxidized alloying elements are in high-enough concentrations to compensate the oxide space charges. It is thus critical to theoretically compute the amount of oxide space charges in these alloys to verify whether the amount of oxidized niobium in solid solution is indeed high enough to obtain an electroneutral oxide, resulting in parabolic kinetics. On the other hand, the amount of oxidized iron would not be sufficient to compensate the oxide space charge, resulting in sub-parabolic kinetics.

OXIDE RESISTIVITY MEASURED BY IN SITU EIS AND RELATION TO HYDROGEN PICKUP FRACTION

The general hypothesis assumes that the oxide resistivity plays a key role in the corrosion mechanism and hydrogen pickup fraction, with the hypothesis that the higher the oxide resistivity, the higher the hydrogen pickup fraction. Thus, Zr-Nb alloys would have a lower oxide resistivity than the Zircaloy-4 alloys.

To validate this hypothesis, in situ EIS was performed on two tube alloys: Zr-2.5Nb and Zircaloy-4. These alloys were selected because of their tube shapes, which fit the EIS experimental setup geometry. Details on the experimental setup, assumptions, and data analysis can be found in Couet et al. [48,49]; thus, only a brief summary is provided herein. The same corrosion conditions were used for the two alloys: 360°C pure water stainless steel autoclave (18MPa; ∼30cc/kg[H_2O] at the beginning of corrosion test by injection of four bars of hydrogen gas). Autoclave electrical feedthroughs were provided by platinum wires in cooled Teflon seal elements at the top of the autoclave. The Zr alloy tubes served as the working electrodes. A perforated platinum cylinder served as a coaxial quasi-reference electrode. This platinum electrode was placed such that an approximate distance of 0.5 mm separated the two electrodes, leading to a symmetrical two-electrode configuration and a negligible ohmic drop across the electrolyte. A two-electrode cell was used because electrochemical reactions at the platinum electrode are much faster than at the Zr electrode, making the platinum electrode a very effective quasi-reference electrode [22]. A platinum/platinum dummy cell of identical geometry was used for electrolyte conductivity monitoring. EIS measurements were acquired at the open-circuit potential at frequencies of approximately 10^{-4} to 10^{6} Hz in a floating configuration ($U_{ac} = 50$ mV) with a PAR4000® potentiostat. The experimental setup has been validated using the dummy-cell and high-temperature electrolytes of theoretically known conductivities [49]. Bode plots were acquired at regular intervals for the two alloys. As has previously been observed [22,50], it was possible to successfully monitor the in situ oxidation kinetics using the capacitance measured at a relatively high frequency (10 kHz) and considering the oxide as a plane capacitor [48,49]. It is worth noting that in the pretransition regime, the in situ EIS oxidation kinetic measurements agreed very well with the weight gain measurements, giving additional confidence in the experimental setup [48,49]. We should also emphasize that the measured corrosion potential was constant over the approximately 300 days of the experiment (except during oxide transitions), as observed by others [22,51].

The apparent oxide resistivity $\rho_{ZrO_2}^{EIS}$ was calculated from the low-frequency impedance measurements multiplied by a geometrical factor:

$$\rho_{ZrO_2}^{EIS} = \frac{\mathrm{Re}(\mathbb{Z}_{\omega \to 0})S}{\delta_{EIS}} \tag{4}$$

where:

$S =$ approximately 8 cm^2 and

$\mathrm{Re}(\mathbb{Z}_{\omega \to 0})$ is averaged over one decade from 300 μHz to 3 mHz.

An average value was chosen as an approximation of $\mathrm{Re}(\mathbb{Z}_{\omega \to 0})$ rather than an interpolation at $\omega = 0$ from the Nyquist diagram because of the significant uncertainty inherent in such an interpolation. Because of this, the measured oxide resistivity represents a value that is lower than the actual oxide resistivity. Note that $\rho_{ZrO_2}^{EIS}$, as calculated using Eq 4, was independent of oxide thickness, whereas the oxide resistance $\mathrm{Re}(\mathbb{Z}_{\omega \to 0})$ increased as the oxide grew. The oxide resistivity (in $10^6\ \Omega \cdot$ cm) at various exposure times for the two alloys is plotted in **Fig. 8** as a function of the f_H^i measured for the two alloys. f_H^i was measured on sister samples taken out of the autoclave at specific exposure intervals Δt ($\Delta t = t_2 - t_1$). $\rho_{ZrO_2}^{EIS}$ was measured at different times in Δt, such that the error bars represent the standard deviations of the EIS measurements in Δt.

The results shown in **Fig. 8** verify the previous assumption that at every exposure time, $\rho_{ZrO_2}^{EIS}$ (Zircaloy-4) was greater than $\rho_{ZrO_2}^{EIS}$ (Zr-2.5Nb). $\rho_{ZrO_2}^{EIS}$ (Zr-2.5Nb) was approximately 3–5 times lower than $\rho_{ZrO_2}^{EIS}$ (Zircaloy-4). Although similar trends have previously been observed [51], this is the first time that a clear relation between $\rho_{ZrO_2}^{EIS}$ and f_H^i has been obtained. It is proposed that as $\rho_{ZrO_2}^{EIS}$ increases from

FIG. 8 Apparent oxide resistivity measured by in situ EIS $\rho^{EIS}_{ZrO_2}$ as a function of instantaneous hydrogen pickup fraction measured on sister samples at similar exposure time intervals.

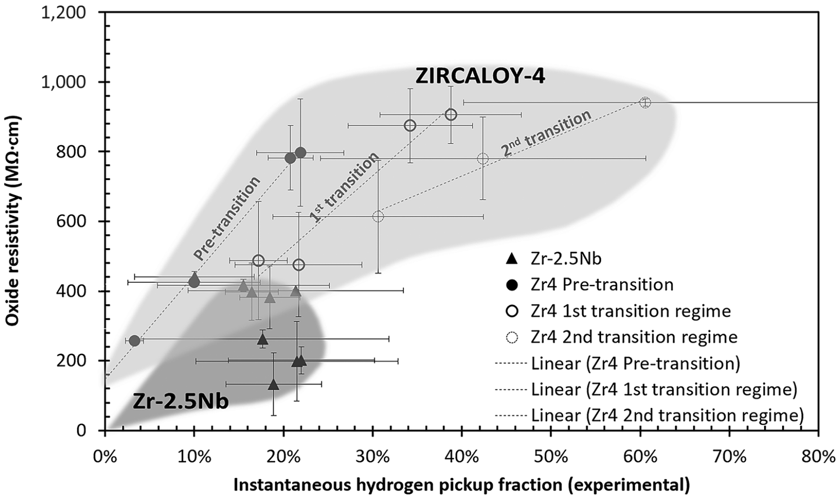

ZrNb to Zircaloy-4 alloys, the electron transport through the oxide layer is more difficult, which increases the electric potential across the oxide, reducing the activation energy for proton absorption at the oxide-water interface. Therefore, oxide resistivity is a key parameter in the hydrogen pickup mechanism and its tuning by the purposeful addition of selected alloying element additions, and careful tailoring of precipitate microstructure is a promising way to limit hydrogen pickup fraction in current and future alloys to be used in the nuclear industry.

The last point is that, in the Zircaloy-4 tube alloy case, the increase in f^t_H from one transition regime to the next (already observed in Fig. 3) did not result in an associated increase in $\rho^{EIS}_{ZrO_2}$. Indeed, as shown in Fig. 8, the dotted lines represent the linear interpolation of $\rho^{EIS}_{ZrO_2}$ as a function of f^i_H for each transition regime. Similar values of $\rho^{EIS}_{ZrO_2}$ were measured at different transition regimes following the periodicity in the oxidation kinetics. This result confirms that a protective oxide grows periodically at the oxide-metal interface. It also confirms that the transport properties of this oxide are similar from one transition regime to the next (because $\rho^{EIS}_{ZrO_2}$ was periodic). This result is also in accordance with the periodic microstructure of the oxide observed using TEM [52], synchrotron radiation [5,53], and a similar in situ EIS setup [22]. Thus, the increase in f^t_H from a transition regime to the next is not due to a change in transport properties of the protective oxide.

The increase would be more probably due to an increase in the proton concentration at the protective-nonprotective oxide interface caused by the overlying porous oxide. Indeed, in the pretransition regime, the hydrogen potential at the protective oxide surface and that in the water are equal. However, when nonprotective oxide layers are present on the top of the growing protective oxide, the hydrogen evolved at the protective oxide surface has to diffuse through these layers to finally reach the water. As a result, a hydrogen potential gradient will be established across the nonprotective oxide layers. This will likely cause proton concentration at the protective oxide surface to increase. Higher concentrations of protons at the protective oxide surface would modify the boundary conditions and could potentially lead to an increase in hydrogen pickup fraction from one transition regime to the next. It is possible, however, that this process will reach steady state after a couple of nonprotective layers are formed such that f_H^t stabilizes and remains constant at longer exposure times (>400 days).

In conclusion, it has been verified that the f_H^t variations between different alloys and different exposure times are correlated to the variations in oxide resistivity. However, although a net increase in $\rho_{ZrO_2}^{EIS}$ was observed as function of exposure time, the underlying process responsible for the apparent alteration of electron transport across the oxide layer was not clearly identified. In addition, although it seems natural to assume that a compensation of oxide space charges results in lower oxide resistivity, this has to be verified theoretically. Thus, it is time to develop a physically based model of Zr alloy corrosion in a high-temperature water environment. This is the purpose of the rest of this paper.

Coupled Current Charge Composition Model

MODEL ASSUMPTIONS

In this section, we describe the corrosion of Zr alloys using the coupled current charge composition (C4) model. This model has already been derived in detail for the case of an electroneutral oxide [20], so only the main assumptions and parameters will be recalled herein. The model arrives at the oxidation kinetics by solving the mobility equations for the atomic species traveling in the oxide layer under concentration and electric potential driving forces. The main hypotheses are as follows:

1. Only the transport of doubly charged oxygen vacancies ($V_{\ddot{O}}$ using Kroger-Vink notations) and electrons (e^-) through the protective oxide layer is considered [4,13,54–58]. Proton diffusion is not modeled.
2. For a given oxide thickness, steady state is assumed, such that the flux of species is constant throughout the oxide [6,20].
3. The concentrations of species at the interfaces are fixed during the exposure time [6,59], resulting in constant interfacial potentials. The constant potential measured during in situ EIS validates this assumption. It is also supposed that the Zr oxide does not dissolve into the electrolyte.
4. The diffusion of oxygen into the metal ahead of the oxide (e.g., to form suboxides ahead of the main oxide front [60,61]) does not significantly affect oxide growth at 360°C.

5. Irradiation effects are not implemented in the model.
6. The oxide-water and oxide-metal interfaces are planar. CRUD effects at the oxide-water interface are not covered.
7. The coupled-current condition of net zero-charge transport through the protective oxide at all times is imposed:

$$\sum_{s}^{\substack{\text{Diffusing}\\ \text{species}}} Z_s e J_s = 2J_{V_{\ddot{O}}} - J_{e^-} = 0 \tag{5}$$

First, an analytical development of the model will be performed for the specific case in which oxide space charges are totally compensated. Then a more general case, including oxide space-charge effects, will be developed.

C4 PARABOLIC OXIDATION MODEL

Using the previously discussed hypotheses, the formulation of the general corrosion model can be solved analytically assuming that electroneutrality is verified locally [62]:

$$\varrho(x) = 0 \Leftrightarrow \sum_{i}^{\substack{\text{Diffusing}\\ \text{species}}} Z_i C_i(x) + \sum_{i}^{\substack{\text{Aliovalent}\\ \text{ions}}} Z_i C_i(x) = 0 \tag{6}$$

It should be noted that whereas oxygen vacancies and electrons are considered diffusing species in Eq 5, the aliovalent ions (such as niobium, iron, and chromium) are not mobile and are only considered in the electroneutrality hypothesis (Eq 6). It is also important to note that the model does not assume that $2C_{V_{\ddot{O}}} = C_{e^-}$.

The space-charge compensation factor Γ is introduced as

$$\Gamma(x) = \left(1 - \frac{\sum_{i}^{\substack{\text{Aliovalent}\\ \text{ions}}} Z_i C_i(x)}{\sum_{i}^{\substack{\text{Diffusing}\\ \text{species}}} Z_i C_i(x)}\right) \tag{7}$$

Basically, if the aliovalent ion charges [equal to $\sum_{i}^{\substack{\text{Aliovalent}\\ \text{ions}}} Z_i C_i(x)$] compensate the diffusing species charge differences [namely the oxide space charges equal to $\sum_{i}^{\substack{\text{Diffusing}\\ \text{species}}} Z_i C_i(x)$], then, using Eq 7, $\Gamma(x) = 0$, whereas if the aliovalent ion charges do not entirely compensate the oxide space charge then $0 < \Gamma(x) \leq 1$.

Eq 6 can be rewritten as function of Γ:

$$\varrho(x) = 0 \Leftrightarrow \Gamma(x) \times \sum_{i}^{\substack{\text{Diffusing}\\ \text{species}}} Z_i C_i(x) = 0 \Leftrightarrow \Gamma(x) = 0 \tag{8}$$

Thus, assuming $\Gamma(x) = 0$, local electroneutrality is verified in the oxide because of the charge compensation effect of oxidized alloying elements incorporated in the oxide (Eq 8). The resolution of the model under these hypotheses leads to the well-known parabolic oxidation kinetics law:

$$\delta_{\Gamma=0}^{C4} = kt^{0.5} \tag{9}$$

A set of parameters shown in **Table 1** has been established and verified previously [20] to best fit the oxidation kinetics of the Zr-0.4Nb alloy that shows nearly parabolic kinetics (Eq 9) during corrosion in 360°C water. Basically, it is considered that (1) the oxide is defect-free at the oxide-water interface; (2) the concentration of oxygen vacancies at the oxide-metal interface is equal to $ZrO_{1.985}$, which corresponds to thermodynamic equilibrium in these conditions [63]; (3) the oxide layer is homogeneous and dense; (4) the oxide-metal interface is electroneutral; and (5) the migration energies come from a best fit of oxidation kinetics and from the literature [20].

Under these conditions, the parabolic scale constant k is equal to $0.35\ \mu m \cdot d^{-1/2}$. This parabolic oxidation law ($\delta_{\Gamma=0}^{C4} = 0.35t^{0.5}$) is plotted in **Fig. 9** along with the heat-treated Zr-1.0Nb and Zircaloy-4 data previously plotted in **Fig. 1**. It is remarkable that $\delta_{\Gamma=0}^{C4}$ agrees very well with the heat-treated Zr-1.0Nb experimental oxide thickness data, as well as the Zr-0.4Nb experimental data (see **Fig. 2**). Thus, the same set of parameters describes very well the Zr-0.4Nb and heat-treated Zr-1.0Nb oxidation kinetics. Of course, as long as $\Gamma = 0$ the oxidation kinetics will remain parabolic, and there is no possibility of reproducing the Zircaloy-4 oxidation kinetics.

The main assumption to obtain a good model for Zr-0.4Nb and heat-treated Zr-1.0Nb oxidation kinetics is that $\Gamma = 0$. Because of this, it is natural to assume that the concentration of oxidized niobium atoms in solid solution embedded in the oxide is indeed high enough to compensate the amount of space charge in the oxide. All niobium atoms are in solid solution in Zr-0.4Nb because 0.4 wt.% is below the niobium

TABLE 1 Values of the different parameters chosen to model Zr-0.4NB oxidation kinetics [20].

Parameters	Value
Electron untrapping energy ($E_m^{e^-}$) in oxide	1 eV
Vacancy migration energy ($E_m^{V_{\ddot{O}}}$) in oxide	1.58 eV
Vacancy migration distance (*a*) in oxide	5 Å
Temperature (*T*)	633 K
Concentration of vacancies at the oxide-metal interface [$C_{V_{\ddot{O}}}(0)$]	4.2×10^{20} vacancies/cm^3
Concentration of electrons at the oxide-metal interface [$C_{e^-}(0)$]	8.4×10^{20} electrons/cm^3
Concentration of vacancies at the oxide-water interface [$C_{V_{\ddot{O}}}(\delta)$]	10^{17} vacancies /cm^3
Concentration of electrons at the oxide-water interface [$C_{e^-}(\delta)$]	10^{17} electrons/cm^3

FIG. 9 Same experimental data as **Fig. 1** (in black) with $\delta^{C4}_{\Gamma=0}$ from Couet, Motta, and Ambard [20] (plotted in red). An expanded view of short exposure times is provided in the lower right corner.

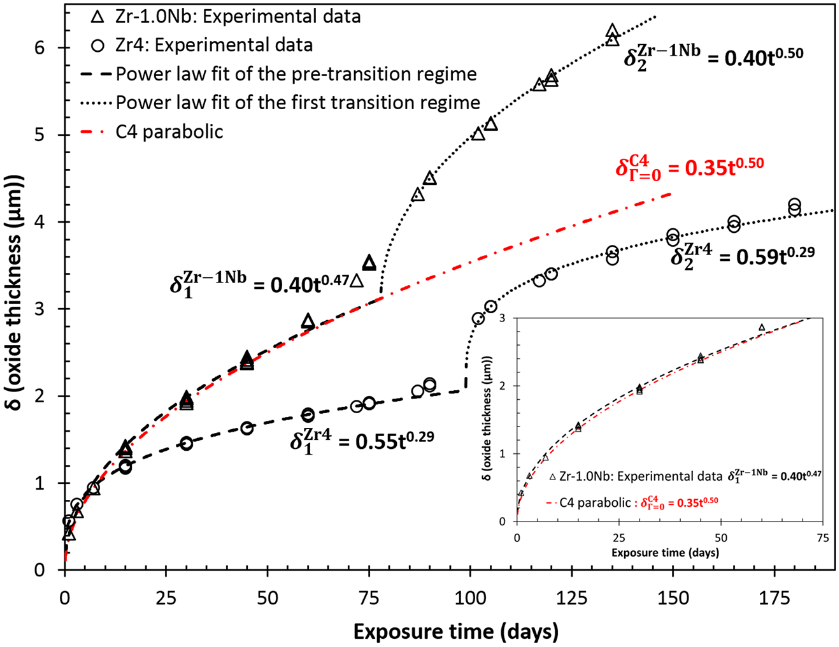

solubility limit in the metal. It is not straightforward to assume the same for Zr-1.0Nb because niobium is typically divided between solid solution and β-niobium precipitates. However, because of the additional heat treatment in the two-phase region, the oxidation kinetics becomes almost parabolic, as seen in **Fig. 1**, and one can assume that the α-Zr grains are saturated with niobium in solid solution. Thus, it is expected that both alloys would present similar oxidation kinetics based on their similar capacity to compensate oxide space charges. It is worth noting that without additional annealing, Zr-1.0Nb oxidation kinetics are sub-parabolic ($n = 0.41$) [64]. It has also been observed previously that ($n = 0.37$) for Zr-2.5Nb alloys. Thus, somehow β-niobium precipitates modify this space-charge compensation mechanism either by modifying the equilibrium concentration of niobium in solid solution or by modifying the transport of charged species through the oxide.

It is possible to compute the concentration of oxidized alloying elements in solid solution necessary to obtain electroneutrality in the oxide, i.e., $\Gamma = 0$.

This concentration $\varpi_{X^{m+}}$ (in wt.%) that is needed to totally compensate the space charge [defined as $\sum_i^{\text{Diffusing species}} Z_iC_i(x)$] is obtained using Eq 10:

$$\varpi_{X^{m+}}(x) = \frac{M_X\left(\sum_i^{\text{Diffusing species}} Z_iC_i(x)\right)}{(4-m)N_A\eta_{ZrO_2}} \tag{10}$$

Thus, the amount in wt.% of Nb^{3+} and Nb^{2+} (and Fe^{3+} and Fe^{2+}) to totally compensate the oxide space charges predicted by the C4 model are plotted in **Fig. 10** as a function of normalized oxide depth as plain (X^{3+}) and dotted (X^{2+}) lines. Of course, less X^{2+} than X^{3+} is needed to compensate the same amount of oxide space charges. **Fig. 10** also shows the XANES results of **Fig. 7**.

It is clearly observed that there is indeed enough oxidized niobium (with an average oxidation state between 2+ and 3+) in solid solution measured by XANES to theoretically totally compensate the oxide space charges computed from the C4 model. Consequently, the XANES data for Zr-0.4Nb verify $\Gamma(x) = 0$ such that Eq 8 is indeed verified and $\delta_{\Gamma=0}^{C4} = 0.35t^{0.5}$ gives very good results in predicting oxidation kinetics of Zr-Nb alloys, as long as no β-niobium precipitates are present.

It should be noted that if Nb^{5+} were present it would increase the oxide space charges and not compensate them, resulting in larger oxidation instabilities. This might be the reason why Nb_2O_5 oxides were not observed experimentally in the oxide bulk. Computational ab initio models would be needed in these highly constrained equilibrium conditions to determine with certainty the stable niobium oxidation state.

FIG. 10 **Fig. 7** with the addition of the curved lines indicating the amount of oxidized niobium and iron in oxide solid solution necessary to obtain $\Gamma = 0$ (i.e., an electroneutral oxide).

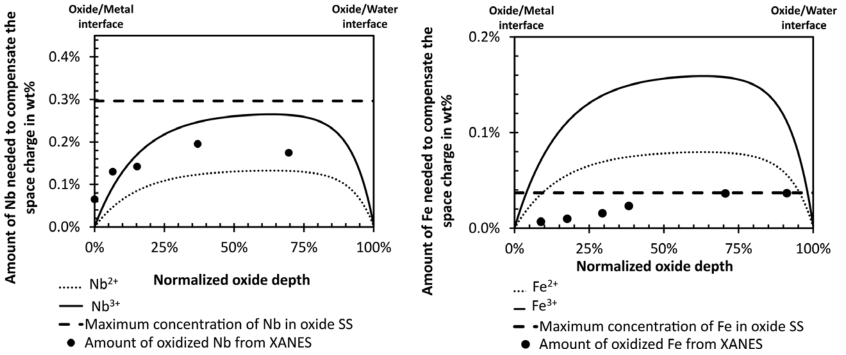

On the other hand, in the case of Zircaloy-4, there is clearly not enough oxidized iron available in oxide solid solution to compensate the oxide space charges. In that case, $\Gamma(x) > 0$ in Eq 8 is not verified, such that, in agreement with the experiment, the C4 parabolic oxidation model cannot be used as it is to predict Zircaloy-4 sub-parabolic oxidation kinetics.

The purpose of the next section is to introduce a more general version of the C4 model in which $0 \leq \Gamma(x) \leq 1$, i.e., in which the oxide space charges induce an extra electric field that modifies the oxidation kinetics.

C4 MODEL WITH OXIDE SPACE-CHARGE EFFECTS $-0 \leq \Gamma(X) \leq 1$

The motivation of this model's derivation was to investigate the effect of $0 < \Gamma(x) \leq 1$ on the oxidation kinetics. Considering the same set of equations and derivations from Couet, Motta, and Ambard [20] developed before the assumption $\Gamma(x) = 0$ was made in Eq 8, one can derive the system of nonlinear equations to be solved. This development is summarized in the Appendix. A current limitation of the model is that for now it is limited to oxide layer thicknesses no larger than 150 nm because of algorithm stability issues at larger oxide thickness (and problem size), which are yet to be resolved.

For simplicity and for lack of better available data, we assumed that $\Gamma(x)$ is constant and independent of the position in the oxide. The oxidation kinetic results up to an oxide thickness of 150 nm are plotted in **Fig. 11** for $\Gamma = 0$, $\Gamma = 0.1$ %, $\Gamma = 1$ %, and $\Gamma = 10$ %. For instance, $\Gamma = 10$ % means that 90 % of the oxide space charges

FIG. 11 Oxidation kinetics showing the effect of Γ on the exponent n of the power law fit. The power law fits are the thin plain lines.

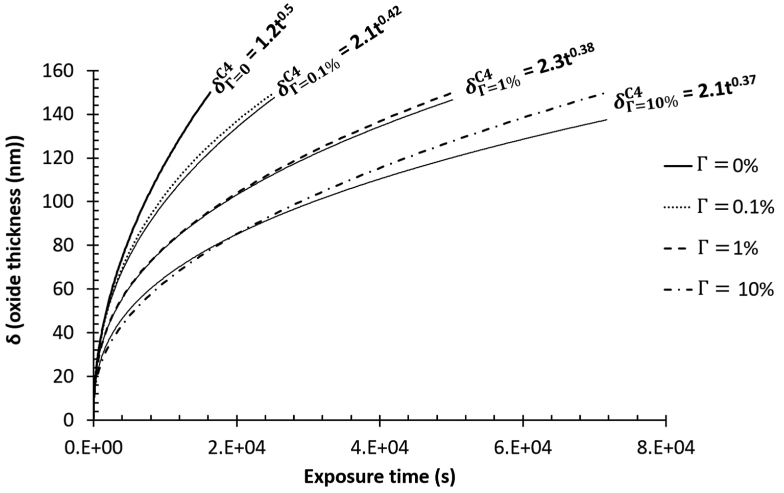

were compensated by aliovalent oxidized ions in oxide solid solution. It is clear that when $\Gamma > 0$, the aliovalent elements can no longer charge compensate, and the oxidation kinetics become sub-parabolic. This effect was more pronounced as the departure from $\Gamma = 0$ increased. Consequently, the oxidation kinetics became more and more sub-parabolic. As a verification, it is noted that for $\Gamma = 0$ the results of this numerical analysis problem are identical to those from the analytical solution provided in **Fig. 9** (the rate constant $1.2\ \mathrm{nm} \cdot \mathrm{s}^{-1/2}$ is equivalent to $0.35\ \mu\mathrm{m} \cdot \mathrm{d}^{-1/2}$). It should be noted that the power law fits are only an approximation of the oxidation kinetics, as observed in **Fig. 11**. Thus, the value of n is merely an approximate empirical tool for evaluating the effects of space charge on experimental data. It is also remarkable that without the introduction of extra parameters (such as oxide stress evolution, oxide cracks, and pore evolution, etc.), the corrosion mechanism in itself predicts sub-parabolic kinetics. In conclusion, space charge of the rate-limiting species (i.e., oxygen vacancies in the sense that $E_m^{\mathrm{V}_{\ddot{\mathrm{O}}}} > E_m^{e^-}$) exerted a retarding effect on the growth rate, leading to apparent sub-parabolic kinetics. This result sheds light onto a major unresolved issue in understanding the corrosion mechanism of Zr alloys, which is to conciliate the widely different oxidation kinetics observed for different Zr alloys showing no significant differences in their oxide microstructure and microchemistry even after extensive oxide microscopy characterizations [53]. Thus, the significant difference in oxidation kinetics observed experimentally between different alloys are qualitatively and quantitatively well explained based on alloying additions.

The next section will introduce the resulting effect on the hydrogen pickup fraction using the apparent oxide resistivity computed from the C4 model.

OXIDE RESISTIVITY CALCULATED BY THE C4 MODEL

The general hypothesis assumes that the oxide resistivity plays a key role in the corrosion mechanism. It has been clearly shown experimentally that as the apparent oxide resistivity increases, the hydrogen pickup fraction increases, and vice versa (**Fig. 8**). According to that hypothesis, Zr-Nb alloys would have a lower apparent oxide resistivity compared with Zircaloy-4 for a given oxide thickness, thus allowing easy electron transport and thus not requiring hydrogen ingress. By apparent oxide resistivity, the oxide resistivity $\rho_{\mathrm{ZrO_2}}$ given by Eq 11 is meant.

$$\rho_{\mathrm{ZrO_2}} = \frac{\Delta V_{\mathrm{OX}}}{J_{e^-}} \tag{11}$$

In that sense, $\rho_{\mathrm{ZrO_2}}$ during corrosion is of course different from bulk crystal $\mathrm{ZrO_2}$ resistivity in nonconstrained equilibrium conditions. The oxide resistivity $\rho_{\mathrm{ZrO_2}}^{\mathrm{C4}}$ was evaluated using the C4 model with the different space-charge compensation factor Γ.

FIG. 12 Apparent oxide resistivity determined by the model $\rho^{C4}_{ZrO_2}$ as a function of oxide thickness for different values of Γ.

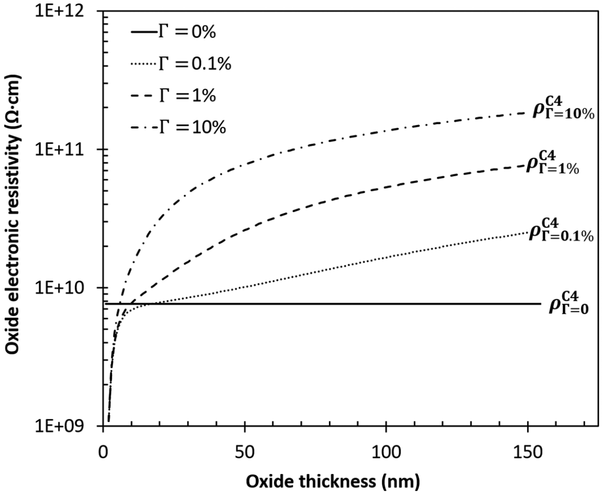

Comparison Between Alloys with Different Space-Charge Compensation Factors

Using the C4 model, it was possible to determine the apparent oxide resistivity (Eq 11) as a function of oxide thickness for different space-charge compensation factors. The results are plotted in Fig. 12. As expected, for a perfect parabolic case defined by $\Gamma = 0$, the oxide resistivity was constant (unfortunately, $\rho^{EIS}_{ZrO_2}$ was only performed on sub-parabolic kinetic Zr-2.5Nb and Zircaloy-4 tube alloys because of experimental setup constraints). However, when oxide space charges were not totally compensated, the apparent oxide resistivity increased significantly. The magnitude of the increase was more significant for higher space-charge compensation factors. Thus, the model also predicted that $\rho^{C4}_{ZrO_2}$ (Zircaloy-4) would be greater than $\rho^{C4}_{ZrO_2}$ (Zr-Nb) because it has already been established that the space-charge compensation factor is greater for Zircaloy-4 than it is for any Zr-Nb alloys. The actual values of the apparent oxide resistivity $\rho^{C4}_{ZrO_2}$ determined by the model were larger by approximately two orders of magnitude than those determined experimentally $\rho^{EIS}_{ZrO_2}$ for two reasons. First, as already stated, $\rho^{EIS}_{ZrO_2}$ is underestimated in the present calculation because of the choice of averaging the impedance at low frequencies rather than interpolating it at zero frequency.

Second, we expect that if the hydrogen flux was modeled in the C4 model, $\rho^{C4}_{ZrO_2}$ would be lower because of the counter effect of hydrogen absorption on its driving force. Indeed, in the C4 formulation, electrons have to migrate across the

FIG. 13 Oxide electric potential (in V) determined by the model $\rho_{ZrO_2}^{C4}$ at 50, 100, and 150 nm as a function of normalized oxide thickness for $\Gamma = 0.1$ %. The results for $\Gamma = 0$ is also plotted (linear line). The arrows indicate increasing oxide thickness.

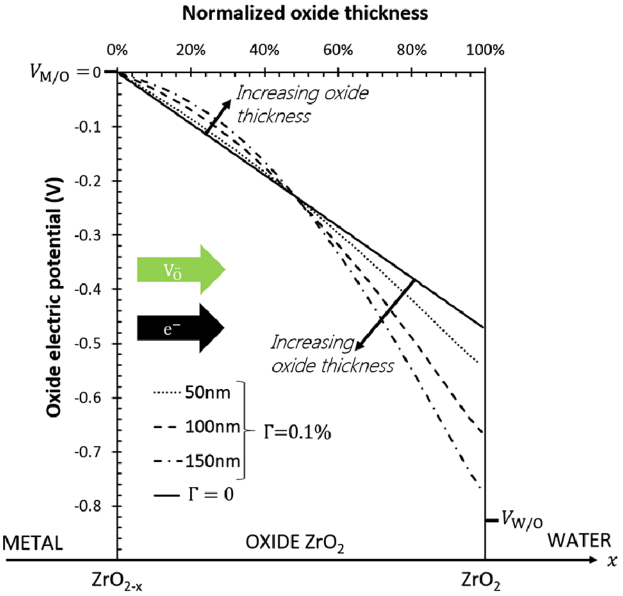

entire oxide. This distance would be lowered if the hydrogen flux was modeled. Thus, $\rho_{ZrO_2}^{C4}$ is overestimated in the current calculation.

In conclusion, the tendency for Zircaloy-4 alloys to absorb more hydrogen at a given oxide thickness compared with Zr-Nb alloys has been demonstrated both experimentally and theoretically based on alloying element additions.

Evolution of Hydrogen Absorption Driving Force as a Function of Exposure Time for a Given Value of the Space-Charge Compensation Factor

Fig. 12 seems to also show that for a given value of $\Gamma > 0$, $\rho_{ZrO_2}^{C4}$ increases as function of oxide thickness (or exposure time), which would suggest that the driving force for hydrogen absorption increases as the oxide grows. The electric potential across the oxide ΔV_{ox} is plotted in Fig. 13 for $\delta = 50$, 100, and 150 nm, respectively, as a function of the normalized oxide thickness for $\Gamma = 0.1$ %. $V_{M/O}$ is arbitrarily set to zero. The result for $\Gamma = 0$ (which is independent of oxide thickness) is also plotted for comparison. The same schematic as in Fig. 6 is also juxtaposed on the plots. It is clearly observed that $|\Delta V_{ox}|$ increases as function of oxide thickness (or exposure time) when $\Gamma = 0.1$ %. This trend is verified for any values of $\Gamma > 0$. This potential increase reduces the activation energy for hydrogen absorption at the oxide-water interface, which leads to an increase in f_H^i, as observed in Fig. 4 and Fig. 5. Thus, the model correctly predicts the increase in f_H^i while the oxide is still protective. The magnitude of the increase in $|\Delta V_{ox}|$ observed in Fig. 13 is once again overestimated by the C4 model because the hydrogen flux is not yet implemented.

Thus, the C4 model verifies the general hypothesis, predicting both an increase in hydrogen pickup fraction for $\Gamma \rightarrow 1$ (explaining the differences between alloys) (Fig. 3) and as a function of exposure time for a given alloy (Fig. 4 and Fig. 5). The differences in oxidation kinetics and hydrogen pickup fraction between alloys are reproduced by the C4 model simply based on the space-charge compensation provided by alloying elements.

Conclusions and Perspectives

Consistent differences in oxidation kinetics (especially in the power law fit exponent *n*) and in hydrogen pickup fraction between different Zr alloys have been noticed since the development of Zr alloys in the 1950s. The proposed model offers a framework for understanding these differences both qualitatively and quantitatively:

1. A general hypothesis based on the effect of alloying element additions on oxide space charges can explain such differences in corrosion kinetics. The cornerstone of this hypothesis is that the higher the oxide space charges, the higher the apparent oxide resistivity and the higher the oxide electric potential, which drives more hydrogen to be absorbed into the metal. The alloying elements embedded in the oxide can act as space-charge compensators depending on their concentrations and oxidation states. By this action, alloying element additions can reduce hydrogen pickup fraction and lead to parabolic oxidation kinetics.
2. The C4 model was developed to verify that hypothesis. The model quantitatively fit the Zr-Nb parabolic oxidation kinetics assuming the space-charge compensation factor was zero, which means that oxide space charges were totally compensated. This is generally the case for Zr-Nb alloys as long as there is enough niobium in oxide solid solution, as verified by μ-XANES. The effect of β-niobium precipitates was unclear but appeared to modify the charge compensation mechanism.
3. In the case of sub-parabolic kinetics observed for Zircaloy-4 alloys, the alloying element concentrations were too small to provide total space-charge compensation (as verified by μ-XANES), such that the space-charge compensation factor was greater than zero.
4. To evaluate the effect of space charges on oxidation kinetics, this component was added to the C4 model. The results indeed show that as the compensation of the oxide space charges decreased, the oxidation kinetics became increasingly subparabolic. Thus, the differences in oxidation kinetics between alloys were caused by differences in the capacity of each alloy to compensate for oxide space charges.
5. Because a comprehensive study also needs to explain variations in hydrogen pickup fraction observed for different Zr alloys, the oxide resistivity was

measured for Zr-2.5Nb and Zircaloy-4 alloys using in situ EIS. The results clearly show that the apparent oxide resistivity of the Zr-2.5Nb alloy was three to five times lower than the Zircaloy-4 alloy. Consequently, according to the general hypothesis, the oxide potential would be higher for Zircaloy-4 alloys, leading to higher hydrogen pickup fraction.

6. In situ EIS results also show that, for a given alloy, the apparent oxide resistivity increased, whereas the oxide was still protective. According to the general hypothesis, this would explain the increase in instantaneous hydrogen pickup fraction observed in every alloy well before the transition happens. This result confirms that oxide resistivity is a key parameter in controlling hydrogen pickup fraction.
7. The apparent oxide resistivity and oxide electric potential were determined using the C4 model. The C4 results qualitatively agreed with the in situ EIS results and show that (1) the less the oxide space charges are compensated, the higher the apparent oxide resistivity is, leading to a higher hydrogen pickup fraction for Zircaloy-4 than for Zr-Nb as observed experimentally; and (2) for a given alloy, the oxide electric potential increases as a function of exposure time, driving more hydrogen to be absorbed as the oxide grows, as shown by the instantaneous hydrogen pickup fraction evolution.

Thus, the C4 model quantitatively and qualitatively predicts the differences observed in oxidation kinetics and hydrogen pickup fraction between different alloys. The compensation effect of solute alloying elements is now well understood. However, the role of precipitates (especially β-niobium) in this framework is unclear and needs to be further investigated.

The oxide resistivity is a key parameter in limiting hydrogen pickup fraction. It is believed that the overall role of the oxide resistivity is to modify the oxide electric potential and thus the activation energy for proton absorption at the oxide-water interface. However, this activation energy would also depend on the absorption site and especially on the local microchemistry. In that sense, it is foreseen that nickel could play a role as a proton getter. In light of these findings, it also natural to expect that irradiation under the forms of electromagnetic waves (ultraviolet, gamma) and neutron could affect the oxide space charges and modify the oxidation kinetics and hydrogen pickup fraction in reactors compared with those seen during autoclave corrosion.

ACKNOWLEDGMENTS

Funding for part of this research was provided by MUZIC-2 (Mechanistic Understanding of Zircaloy Corrosion) Research Consortium. We are grateful for helpful discussions with Christophe Domain and Martin Bachet as well as for technical support from Didier Livigni and Thierry Ghys and with the community of the MUZIC-2 research program. We would also like to thank Zhonghou Cai for his expert assistance during the μ-XANES experiments at APS. Usage of the APS was supported by the U.S. Department of Energy under Contract No. DE-AC02-06CH11357.

Appendix

The oxide layer is discretized into N layers as shown in **Fig. A1**. In **Fig. A1**, one can clearly observe that the mobility of species s is dependent not only on the migration energy of species E_m^s but also on the local electric field E_k, where E_k is given by Eq A1

$$\begin{aligned} E_k &= E_0 + \frac{8\pi ae}{\varepsilon\varepsilon_0}\Gamma_k \sum_{l=1}^{k}\left(2C_l^{\mathrm{V\ddot{O}}} - C_l^{e^-}\right) = E_0 + \Gamma_k \epsilon_k, \\ \text{with } \Gamma_k &= \left(1 - \frac{\sum_i^{\substack{\text{Aliovalent}\\ \text{ions}}} Z_i C_i(x_k)}{\sum_i^{\substack{\text{Diffusing}\\ \text{species}}} Z_i C_i(x_k)}\right) \text{ and } \epsilon_k = \frac{8\pi ae}{\varepsilon\varepsilon_0}\sum_{l=1}^{k}\left(2C_l^{\mathrm{V\ddot{O}}} - C_l^{e^-}\right) \end{aligned} \tag{A1}$$

where:
Γ_k = space-charge compensation factor as defined in Eq 7 evaluated at the kth layer [62].

Assuming Boltzmann statistics and steady state, the particle current J^s is equal to

$$J^s = 2av_s \mathrm{e}^{-\left(\frac{eE_m^s}{k_B T}\right)}\left(C_{k-1}^s \mathrm{e}^{\frac{Z_s eaE_k}{k_B T}} - C_k^s \mathrm{e}^{\frac{Z_s eaE_k}{k_B T}}\right) \tag{A2}$$

The system of equations contains $2N - 1$ unknowns: $2(N - 1)$ concentrations—the ones at the boundaries are known (see **Table 1**)—and the homogeneous field E_0. Hopefully, the system also contains $2N - 1$ nonlinear equations: $2(N - 1)$ flux equations (Eq A2) due to the steady-state assumption $J_{k-1}^s = J_k^s$ (for $V_{\ddot{O}}$ [Eq A3] and e^-

FIG. A1 Scheme of the discrete lattice and the potential energy diagram in the case of Zr corrosion. The oxidation process can be conceptually divided into several steps as presented.

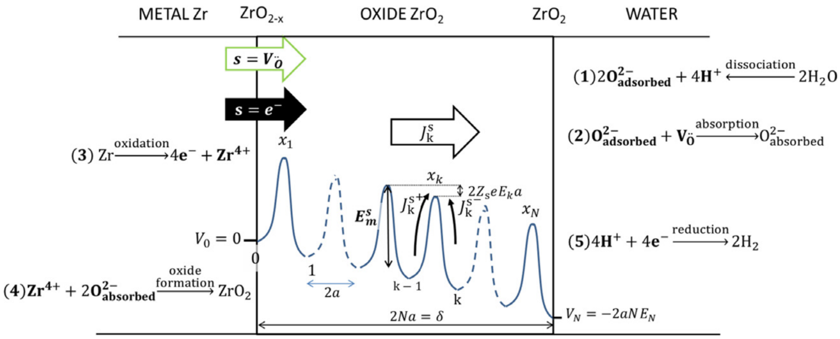

[Eq A4]) and the coupled current Eq 5 written explicitly in Eq A5. Thus, one can solve this system of nonlinear equations, which is defined as follows:

$$
\begin{cases}
\begin{cases}
\text{For k=2 to N:} \\
\left(C_{k-2}^{\mathrm{V}_{\ddot{\mathrm{O}}}} e^{\frac{2ea\left(E_0+\Gamma_{k-1}\epsilon_{k-1}\right)}{k_B T}} - C_{k-1}^{\mathrm{V}_{\ddot{\mathrm{O}}}} e^{-\left(\frac{2ea\left(E_0+\Gamma_{k-1}\epsilon_{k-1}\right)}{k_B T}\right)}\right) \\
\qquad -\left(C_{k-1}^{\mathrm{V}_{\ddot{\mathrm{O}}}} e^{\frac{2ea\left(E_0+\Gamma_{k}\epsilon_{k}\right)}{k_B T}} - C_{k}^{\mathrm{V}_{\ddot{\mathrm{O}}}} e^{-\left(\frac{2ea\left(E_0+\Gamma_{k}\epsilon_{k}\right)}{k_B T}\right)}\right) = 0 & \text{(A3)} \\
\left(C_{k-2}^{e^-} e^{\frac{-ea\left(E_0+\Gamma_{k-1}\epsilon_{k-1}\right)}{k_B T}} - C_{k-1}^{e^-} e^{\frac{ea\left(E_0+\Gamma_{k-1}\epsilon_{k-1}\right)}{k_B T}}\right) \\
\qquad -\left(C_{k-1}^{e^-} e^{\frac{-ea\left(E_0+\Gamma_{k}\epsilon_{k}\right)}{k_B T}} - C_{k}^{e^-} e^{\frac{ea\left(E_0+\Gamma_{k}\epsilon_{k}\right)}{k_B T}}\right) = 0 & \text{(A4)}
\end{cases} \\
2\nu_{\mathrm{V}_{\ddot{\mathrm{O}}}} e^{-\left(\frac{E_m^{\mathrm{V}_{\ddot{\mathrm{O}}}}}{k_B T}\right)} \left(C_{0}^{\mathrm{V}_{\ddot{\mathrm{O}}}} e^{\frac{2ea\left(E_0+\Gamma_{1}\epsilon_{1}\right)}{k_B T}} - C_{1}^{\mathrm{V}_{\ddot{\mathrm{O}}}} e^{-\left(\frac{2ea\left(E_0+\Gamma_{1}\epsilon_{1}\right)}{k_B T}\right)}\right) \\
\qquad -\nu_{e^-} e^{-\left(\frac{E_m^{e^-}}{k_B T}\right)} \left(C_{0}^{e^-} e^{\frac{-ea\left(E_0+\Gamma_{k}\epsilon_{k}\right)}{k_B T}} - C_{1}^{e^-} e^{\frac{ea\left(E_0+\Gamma_{1}\epsilon_{1}\right)}{k_B T}}\right) = 0 & \text{(A5)}
\end{cases}
$$

This system can be rewritten in a vector-like fashion using

$$
\Lambda = \left[C_1^{e^-}, C_1^{\mathrm{V}_{\ddot{\mathrm{O}}}}, C_2^{e^-}, C_2^{\mathrm{V}_{\ddot{\mathrm{O}}}}, \cdots C_{N-1}^{e^-}, C_{N-1}^{\mathrm{V}_{\ddot{\mathrm{O}}}}, E_0\right] \tag{A6}
$$

which gives

$$
\mathrm{F}(\Lambda) = \left[\begin{array}{c}
\begin{cases}
\text{For } k = 2 \text{ to } N\text{:} \\
f_k^{\mathrm{V}_{\ddot{\mathrm{O}}}}(C_1^{e^-}, C_1^{\mathrm{V}_{\ddot{\mathrm{O}}}}, C_2^{e^-}, C_2^{\mathrm{V}_{\ddot{\mathrm{O}}}}, \ldots, C_{N-1}^{e^-}, C_{N-1}^{\mathrm{V}_{\ddot{\mathrm{O}}}}, E_0 \\
f_k^{e^-}(C_1^{e^-}, C_1^{\mathrm{V}_{\ddot{\mathrm{O}}}}, C_2^{e^-}, C_2^{\mathrm{V}_{\ddot{\mathrm{O}}}}, \ldots, C_{N-1}^{e^-}, C_{N-1}^{\mathrm{V}_{\ddot{\mathrm{O}}}}, E_0
\end{cases} \\
f_{cc}(C_1^{e^-}, C_1^{\mathrm{V}_{\ddot{\mathrm{O}}}}, E_0)
\end{array}\right] = 0 \tag{A7}
$$

Thus, $\mathrm{F}(\Lambda)$ is a $(2N-1)^2$ matrix and the problem is equivalent to solving $\mathrm{F}(\Lambda) = 0$. This system of nonlinear equations can be solved using a robust Newtonian method. The LU decomposition provided by the "dgesv" module of the LAPACK library has been used [65].

The continuous functions are as a function of x, the distance from the oxide-metal interface. The discretized functions are as a function of k, the discretized position in the oxide denoted by x_k, the distance from oxide-metal interface, with k the number of oxide monolayers from the oxide-metal interface. See **Table A1** for definitions of variables and parameters.

TABLE A1 Definitions of variables and parameters.

δ	Oxide thickness from weight gain measurements (m)
δ_{EIS}	Oxide thickness from in situ EIS measurements (m)
t	Exposure time (s)
n	Exponent of oxidation power law fit
k	Scaling constant of oxidation power law fit ($m \cdot s^{1/n}$)
f_H^t	Total hydrogen pickup fraction
f_H^i	Instantaneous hydrogen pickup fraction
s	Species (e.g., electrons, oxygen vacancies, etc.)
Z_s	Electric charge of the species s
$V_{\ddot{O}}$	Oxygen vacancy in a Kroger-Vink notation (charge +2)
e^-	Electron (charge −1)
S	Sample surface (m^2)
ω	EIS signal frequency ($rad \cdot s^{-1}$)
$\mathrm{Re}(\mathbb{Z}_{\omega \to 0})$	Real impedance as the EIS frequency tends toward zero (Ω)
e	Elementary charge (C)
J_s or J^s	Species' flux in the oxide ($species \cdot cm^{-2} \cdot s^{-1}$)
ϱ	Volume charge density in ($C \cdot m^{-3}$)
C_s	Concentration of species s ($species \cdot m^3$)
Γ	Space-charge compensation factor
X	Aliovalent ion in oxide solid solution (e.g., niobium, iron, etc.)
M_X	Molar mass of X ($g \cdot mol^{-1}$)
η_{ZrO_2}	Density of ZrO_2 ($g \cdot m^{-3}$)
m	Oxidation state of the aliovalent ion in solid solution
$\varpi_{X^{m+}}$	Amount of X^{m+} (in wt.%) in solid solution in the oxide needed to totally compensate the space charge
N_A	Avogadro's number ($species \cdot mol^{-1}$)
E_O	Oxide-metal interface (also called homogeneous) electric field ($V \cdot m^{-1}$)
E	Electric field in the oxide [$V \cdot m^{-1}$]
N	Total number of oxide monolayers
E_m^s	Migration energy of species s (eV)
$2a$	Jump distance between two potential minima in the oxide (m)
ε_O	Vacuum permittivity ($F \cdot m^{-1}$)
ε	Relative permittivity of ZrO_2
ν_s	Jump frequency of the species s (s^{-1})
T	Temperature (K)
k_B	Boltzmann's constant ($eV \cdot K^{-1}$)
ΔV_{ox}	Electric potential across the oxide (V)

References

[1] Motta, A. T., Couet, A., and Comstock, R. J., “Corrosion of Zirconium Alloys Used for Nuclear Fuel Cladding,” *Ann. Rev. Mater. Res.*, Vol. 45, 2015, pp. 311–343.

[2] Cox, B., “A Mechanism for the Hydrogen Uptake Process in Zirconium Alloys,” *J. Nucl. Mater.*, Vol. 264, No. 3, 1999, pp. 283–294.

[3] Couet, A., Motta, A. T., and Comstock, R. J., “Hydrogen Pickup Measurements in Zirconium Alloys: Relation to Oxidation Kinetics,” *J. Nucl. Mater.*, Vol. 451, Nos. 1–3, 2014, pp. 1–13.

[4] Porte, H. A., Schnizlein, J. G., Vogel, R. C., and Fischer, D. F., “Oxidation of Zirconium and Zirconium Alloys,” *J. Electrochem. Soc.*, Vol. 107, No. 6, 1960, pp. 506–515.

[5] Motta, A. T., Gomes da Silva, M. J., Yilmazbayhan, A., Comstock, R. J., Cai, Z., and Lai, B., “Microstructural Characterization of Oxides Formed on Model Zr Alloys Using Synchrotron Radiation,” *Zirconium in the Nuclear Industry, ASTM STP1505*, B. Kammenzind and M. Limbäck, Eds., ASTM International, West Conshohocken, PA, 2009, pp. 486–506.

[6] Tupin, M., Pijolat, M., Valdivieso, F., Soustelle, M., Frichet, A., and Barberis, P., “Differences in Reactivity of Oxide Growth during the Oxidation of Zircaloy-4 in Water Vapour Before and after the Kinetic Transition,” *J. Nucl. Mater.*, Vol. 317, Nos. 2–3, 2003, pp. 130–144.

[7] Kass, S., “The Development of the Zircaloys,” presented at *USAEC Symposium on Zirconium Alloy Development, GEAP-4089*, Castlewood, Pleasanton, CA, November 12–14, 1962—unpublished.

[8] Kiselev, A. A., *Research on the Corrosion of Zirconium Alloys in Water and Steam at High Temperature and Pressure*, Atomic Energy of Canada Ltd., Chalk River, Canada, 1963.

[9] Kass, S. and Kirk, W. W., “Corrosion and Hydrogen Absorption Properties of Nickel-Free Zircaloy-2 and Zircaloy-4,” *ASM Trans. Quart.*, Vol. 56, 1962, pp. 77–100.

[10] Murgatroyd, B. A. and Winton, J., “Hydriding Zircaloy-2 in Lithium Hydroxide Solutions,” *J. Nucl. Mater.*, Vol. 23, No. 3, 1967, pp. 249–256.

[11] Couet, A., Motta, A. T., Comstock, R. J., and Paul, R. L., “Cold Neutron Prompt Gamma Activation Analysis, a Non-Destructive Technique for Hydrogen Level Assessment in Zirconium Alloys,” *J. Nucl. Mater.*, Vol. 425, Nos. 1–3, 2012, pp. 211–217.

[12] Cox, B., “Some Thoughts on the Mechanisms of In-Reactor Corrosion of Zirconium Alloys,” *J. Nucl. Mater.*, Vol. 336, Nos. 2–3, 2005, pp. 331–368.

[13] Cox, B., “Low Temperature (Inferior to 300°C) Oxidation of Zircaloy-2 in Water,” *J. Nucl. Mater.*, Vol. 25, No. 3, 1968, pp. 310–321.

[14] Arima, T., Moriyama, K., Gaja, N., Furuya, H., Idemitsu, K., and Inagaki, Y., “Oxidation Kinetics of Zircaloy-2 Between 450°C and 600°C in Oxidizing Atmosphere,” *J. Nucl. Mater.*, Vol. 257, No. 1, 1998, pp. 67–77.

[15] Dawson, J. K., Long, G., Seddon, W. E., and White, J. F., “The Kinetics and Mechanism of the Oxidation of Zircaloy-2 at 350–500°C,” *J. Nucl. Mater.*, Vol. 25, No. 2, 1968, pp. 179–200.

[16] Wagner, C. and Schottky, W., "Theory of Controlled Mixed Phases," Zeitschrift für Physikalische Chemie, Abteilung B: Chemie der Elementarprozesse, Aufbau der Materie B11, 1930, pp. 163–210.

[17] Hauffe, K., *Oxidation of Metals*, Plenum Press, Berlin, Germany, 1965.

[18] Zumpicchiat, G., Pascal, S., Tupin, M., and Berdin-Méric, C., "Finite Element Modelling of the Oxidation Kinetics of Zircaloy-4 with a Controlled Metal-Oxide Interface and the Influence of Growth Stress," *Corr. Sci.*, Vol. 100, 2015, pp. 209–221.

[19] Eloff, G. A., Greyling, C. J., and Viljoen, P. E., "The Role of Space Charge in the Oxidation of Zircaloy-4 between 350 and 450°C in Air," *J. Nucl. Mater.*, Vol. 199, No. 3, 1993, pp. 285–288.

[20] Couet, A., Motta, A. T., and Ambard, A., "The Coupled Current Charge Compensation Model for Zirconium Alloy Fuel Cladding Oxidation: I. Parabolic Oxidation of Zirconium Alloys," *Corr. Sci.*, Vol. 100, 2015, pp. 73–84.

[21] Bryner, J. S., "Cyclic Nature of Corrosion of Zircaloy-4 in 633K Water," *J. Nucl. Mater.*, Vol. 82, No. 1, 1979, pp. 84–101.

[22] Schefold, J., Lincot, D., Ambard, A., and Kerrec, O., "The Cyclic Nature of Corrosion of Zr and Zr-Sn in High-Temperature Water (633 K): A Long-Term In Situ Impedance Spectroscopic Study," *J. Electrochem. Soc.*, Vol. 150, No. 10, 2003, pp. B451–B461.

[23] Abriata, J. P. and Bolcich, J. C., "The Nb-Zr (Niobium-Zirconium) System," *Journal of Phase Equilibria*, Vol. 3, No. 1, 1982, pp. 34–44.

[24] Hu, J., Setiadinata, B., Aarholt, T., Garner, A., Vilalta-Clemente, A., Partezana, J., Frankel, P., Bagot, P., Lozano-Perez, S., Wilkinson, A., Preuss, M., Moody, M., and Grovenor, C., "Understanding Corrosion and Hydrogen Pickup of Zirconium Fuel Cladding Alloys: The Role of Oxide Microstructure, Porosity, Suboxide, and Second-Phase Particles," *Zirconium in the Nuclear Industry: 18th International Symposium, ASTM STP1597*, R. J. Comstock and A. T. Motta, Eds., ASTM International, West Conshohocken, PA, 2018, pp. 93–126.

[25] Cox, B. and Roy, C., *The Use of Tritium as a Tracer in Studies of Hydrogen Uptake by Zirconium Alloys*, Atomic Energy of Canada Ltd., Chalk River, Canada, 1965.

[26] Sabol, G. P., Kilp, G. R., Balfour, M. G., and Roberts, E., "Development of a Cladding Alloy for High Burnup," *Zirconium in the Nuclear Industry: Eighth International Symposium, ASTM STP1023*, C. M. Eucken and L. F. P. Van Swam, Eds., ASTM International, Philadelphia, PA, 1989, pp. 227–244.

[27] Thomazet, J., Dalmais, A., Bossis, P., Godlewski, J., Blat, M., and Miquet, A., "The Corrosion of the Alloy M5: An Overview," presented at *IAEA Technical Committee Meeting on Behavior of High Corrosion Resistance Zr-Based Alloys*, Buenos Aires, Argentina, October 24–28, 2005, pp. 77–98.

[28] Une, K., Sakamoto, K., Aomi, M., Matsunaga, J., Etoh, Y., Takagi, I., Miyamura, S., Kobayashi, T., and Ito, K., "Hydrogen Absorption Mechanism of Zirconium Alloys Based on Characterization of Oxide Layer," *Zirconium in the Nuclear Industry: 16th International Symposium, ASTM STP1529*, M. Limbäck and B. Pierre, Eds., ASTM International, West Conshohocken, PA, 2011, pp. 401–432.

[29] Harada, M. and Wakamatsu, R., "The Effect of Hydrogen on the Transition Behavior of the Corrosion Rate of Zirconium Alloys," *Zirconium in the Nuclear Industry: 15th International Symposium, ASTM STP1505*, B. Kammenzind and M. Limbäck, Eds., ASTM International, West Conshohocken, PA, 2008, pp. 384–400.

[30] Couet, A., Motta, A. T., and Comstock, R. J., "Effect of Alloying Elements on Hydrogen Pick-Up in Zirconium Alloys," *Zirconium in the Nuclear Industry: 17th Volume, ASTM STP1543*, B. Comstock, Ed., ASTM International, West Conshohocken, PA, 2013, pp. 479–514.

[31] Beie, H.-J., Mitwalsky, A., Garzarolli, F., Ruhmann, H., and Sell, H. J., "Examinations of the Corrosion Mechanism of Zirconium Alloys," *Zirconium in the Nuclear Industry: Tenth International Symposium, ASTM STP1245*, A. M. Garde and E. R. Bradley, Eds., ASTM International, Philadelphia, PA, 1994, pp. 615–643.

[32] Gohr, H., Schaller, J., Ruhmann, H., and Garzarolli, F., "Long-Term In Situ Corrosion Investigation of Zr Alloys in Simulated PWR Environment by Electrochemical Measurements," *Zirconium in the Nuclear Industry: Eleventh International Symposium, ASTM STP1295*, E. R. Bradley and G. P. Sabol, Eds., ASTM International, West Conshohocken, PA, 1996, pp. 181–202.

[33] Kofstad, P., *Nonstoichiometry, Diffusion, and Electrical Conductivity in Binary Metal Oxides*, Wiley-Interscience, New York, 1972.

[34] Kofstad, P., "Effect of Impurities on Defect in Oxides and Their Relationship to Oxidation of Metal," *Corrosion*, Vol. 24, No. 11, 1968, pp. 379–388.

[35] Fromhold, A. T., *Theory of Metal Oxidation: Space Charge*, North-Holland, Amsterdam, the Netherlands, 1980.

[36] Fromhold, A. T., "Easy Insight into Space-Charge Effects on Steady-State Transport in Oxide-Films," *Oxid. Metals*, Vol. 13, No. 5, 1979, pp. 475–479.

[37] Yilmazbayhan, A., Delaire, O., Motta, A. T., Birtcher, R. C., Maser, J. M., and Lai, B., "Determination of the Alloying Content in the Matrix of Zr Alloys Using Synchrotron Radiation Microprobe X-Ray Fluorescence," *J. Nucl. Mater.*, Vol. 321, Nos. 2–3, 2003, pp. 221–232.

[38] Pêcheur, D., Filippov, V. P., Bateev, A. B., and Ivanov, J. J., "Mossbauer Investigations of the Chemical States of Tin and Iron Atoms in Zirconium Alloy Oxide Film," *Zirconium in the Nuclear Industry: Thirteenth International Symposium, ASTM STP1423*, G. D. Moan and P. Rudling, Eds., ASTM International, West Conshohocken, PA, 2002, pp. 135–153.

[39] Anada, H., Takeda, K., Nasu, S., and Nakamichi, T., "Chemical State Analysis of Sn and Fe in ZrO_2 by Mossbauer Spectroscopy," *Zirconium in the Nuclear Industry: Thirteenth International Symposium, ASTM STP1423*, G. D. Moan and P. Rudling, Eds., ASTM International, West Conshohocken, PA, 2001, pp. 154–168.

[40] Hulme, H., Preuss, M., Lyon, S., Steuwer, A., Noren, K., Carlson, S., Wei, J., Ivermark, M., and Comstock, R. J., "A Study of the Oxidation State of Tin in Zirconium Alloy Oxides Using XANES," presented at *Universities Nuclear Technology Forum*, Oxford University, Oxford, UK, April 14–16, 2014—unpublished.

[41] Couet, A., Motta, A. T., de Gabory, B., and Cai, Z., "Microbeam X-Ray Absorption Near-Edge Spectroscopy Study of the Oxidation of Fe and Nb in Zirconium Alloy Oxide Layers," *J. Nucl. Mater.*, Vol. 452, Nos. 1–3, 2014, pp. 614–627.

[42] Loucif, K., Merle, P., and Borrelly, R., "On the Thermoelectric Power Variation According to Temperature of Zirconium Alloys and Its Possible Application to the Estimation of the Amount of Solubility Variations of Iron and Chromium in Zircaloy," *J. Nucl. Mater.*, Vol. 202, Nos. 1–2, 1993, pp. 193–196.

[43] Borrelly, R., Merle, P., and Adami, L., "Study of the Solubility of Iron in Zirconium by Thermoelectric Power Measurements," *J. Nucl. Mater.*, Vol. 170, No. 2, 1990, pp. 147–156.

[44] Li, C., Zhou, B., Zhou, W., Li, P., Peng, Q., Ying, S., and Shen, B., "Determination of Fe and Cr Content in α-Zr Solid Solution of Zircaloy-4 with Different Heat-Treated States," *J. Nucl. Mater.*, Vol. 304, Nos. 2–3, 2002, pp. 134–138.

[45] Sakamoto, K., Une, K., Aomi, M., Otsuka, T., and Hashizume, K., "Change of Chemical States of Niobium in the Oxide Layer of Zirconium-Niobium Alloys with Oxide Growth," *J. Nucl. Sci. Techn.*, Vol. 52, No. 10, 2015, pp. 1259–1264.

[46] Sakamoto, K., Une, K., Aomi, M., and Hashizume, K., "Oxidation Behavior of Niobium in Oxide Layers of Zirconium-Niobium Alloys", presented at *TopFuel 2012*, Manchester, UK, September 2–6, 2012, pp. 297–306.

[47] Froideval, A., Degueldre, C., Segre, C. U., Pouchon, M. A., and Grolimund, D., "Niobium Speciation at the Metal/Oxide Interface of Corroded Niobium-Doped Zircaloys: A X-Ray Absorption Near-Edge Structure Study," *Corr. Sci.*, Vol. 50, No. 5, 2008, pp. 1313–1320.

[48] Couet, A., Motta, A. T., Ambard, A., and Comstock, R. J., "Oxide Electronic Conductivity and Hydrogen Pickup Fraction in Zr Alloys," presented at the *ANS Annual Meeting*, Reno, NV, June 15–19, 2014, pp. 845–848.

[49] Couet, A., Motta, A. T., Ambard, A., and Livigni, D., "In-Situ Electrochemical Impedance Spectroscopy Measurements of Zirconium Alloy Oxide Conductivity: Relationship to Hydrogen Pickup," *Corr. Sci.*, Vol. 119, 2017, pp. 1–13.

[50] Tupin, M., Bataillon, C., Gozlan, J.-P., and Bossis, P., "High Temperature Corrosion of Zircaloy-4," *Electrochemistry in Light Water Reactors: Reference Electrodes, Measurement, Corrosion and Tribocorrosion Issues*, R. W. Bosch, D. Féron, and J. P. Celis, Eds., 2007, European Federation for Corrosion, London, pp. 134–163.

[51] Baur, K., Garzarolli, F., Ruhmann, H., and Sell, H.-J., "Electrochemical Examinations in 350°C Water with Respect to the Mechanism of Corrosion-Hydrogen Pickup," *Zirconium in the Nuclear Industry: Twelfth International Symposium, ASTM STP1354*, G. P. Sabol and G. D. Moan, Eds., ASTM International, West Conshohocken, PA, 2000, pp. 836–852.

[52] Garner, A., Gholinia, A., Frankel, P., Gass, M., MacLaren, I., and Preuss, M., "The Microstructure and Microtexture of Zirconium Oxide Films Studied by Transmission Electron Backscatter Diffraction and Automated Crystal Orientation Mapping with Transmission Electron Microscopy," *Acta Mater.*, Vol. 80, 2014, pp. 159–171.

[53] Yilmazbayhan, A., Motta, A. T., Comstock, R. J., Sabol, G. P., Lai, B., and Cai, Z., "Structure of Zirconium Alloy Oxides Formed in Pure Water Studied with Synchrotron Radiation and Optical Microscopy: Relation to Corrosion Rate," *J. Nucl. Mater.*, Vol. 324, No. 1, 2004, pp. 6–22.

[54] Kofstad, P. and Ruzicka, D. J., "On the Defect Structure of ZrO_2 And HfO_2," *J. Electrochem. Soc.*, Vol. 110, No. 3, 1963, pp. 181–184.

[55] Belle, J. and Mallett, M. W., "Kinetics of the High Temperature Oxidation of Zirconium," *J. Electrochem. Soc.*, Vol. 101, No. 7, 1954, pp. 339–342.

[56] Lustman, B. and Kerze, F., *The Metallurgy of Zirconium*, McGraw-Hill, New York, 1955.

[57] Grandjean, A. and Serruys, Y., "Metal and Oxygen Mobilities during Zircaloy-4 Oxidation at High Temperature," *J. Nucl. Mater.*, Vol. 273, No. 1, 1999, pp. 111–115.

[58] Bojinov, M., Karastoyanov, V., Kinnunen, P., and Saario, T., "Influence of Water Chemistry on the Corrosion Mechanism of a Zirconium-Niobium Alloy in Simulated Light Water Reactor Coolant Conditions," *Corr. Sci.*, Vol. 52, No. 1, 2010, pp. 54–67.

[59] Dali, Y., Tupin, M., Bossis, P., Pijolat, M., Wouters, Y., and Jomard, F., "Corrosion Kinetics under High Pressure of Steam of Pure Zirconium and Zirconium Alloys Followed by In Situ Thermogravimetry," *J. Nucl. Mater.*, Vol. 426, Nos. 1–3, 2012, pp. 148–159.

[60] de Gabory, B., Dong, Y., Motta, A. T., and Marquis, E. A., "EELS and Atom Probe Tomography Study of the Evolution of the Metal/Oxide Interface during Zirconium Alloy Oxidation," *J. Nucl. Mater.*, Vol. 462, 2015, pp. 304–309.

[61] Ni, N., Hudson, D., Wei, J., Wang, P., Lozano-Perez, S., Smith, G. D. W., Sykes, J. M., Yardley, S. S., Moore, K. L., Lyon, S., Cottis, R., Preuss, M., and Grovenor, C. R. M., "How the Crystallography and Nanoscale Chemistry of the Metal/Oxide Interface Develops during the Aqueous Oxidation of Zirconium Cladding Alloys," *Acta Mater.*, Vol. 60, No. 20, 2012, pp. 7132–7149.

[62] Fromhold, A. T., "Parabolic Oxidation of Metals in Homogeneous Electric-Fields," *J. Phys. Chem. Solids*, Vol. 33, No. 1, 1972, pp. 95–120.

[63] Ma, X., Toffolon-Masclet, C., Guilbert, T., Hamon, D., and Brachet, J. C., "Oxidation Kinetics and Oxygen Diffusion in Low-Tin Zircaloy-4 up to 1523 K," *J. Nucl. Mater.*, Vol. 377, 2008, pp. 359–369.

[64] Romero, J., Partezana, J., Comstock, R. J., Hallstadius, L., Motta, A. T., and Couet, A., "Evolution of Hydrogen Pickup Fraction with Oxidation Rate on Zirconium Alloys," presented at *TopFuel 2015*, Zurich, Switzerland, September 13–17, 2015—unpublished.

[65] Anderson, E., Bai, Z., Dongarra, J., Greenbaum, A., McKenney, A., Croz, J. D., Hammerling, S., Demmel, J., Bischof, C., and Sorensen, D., "LAPACK: A Portable Linear Algebra Library for High-Performance Computers," presented at *Proceedings of the ACM/IEEE Conference on Supercomputing*, New York, November 12–16, 1990, pp. 2–11.

Discussion

Question from Ron Adamson, Zircology Plus:—Can you comment on the possibility that the nature or magnitude of the space charge is changed by irradiation—perhaps because irradiation may change the electrical conductivity of the oxide. The effect is not necessarily related to dpa (which induces changes in the chemical structure of the second-phase particles) but to instantaneous effects of neutrons, gamma, etc.

Authors' Response:—We believe that irradiation (both neutrons and photons) would induce changes in space charge in the oxide. For instance, neutron damage will certainly increase the concentration of defects in the oxide. Although the formation of a Frenkel pair is electroneutral in nature, there is a probability that the knock on interstitials will be out of range from the vacancy recombination volume (although the local electric field will induce a larger recombination volume than in metals). The surviving interstitials and vacancies are charged defects and will contribute to local space charge. On the other hand, photons from the ultraviolet to gamma rays, have enough energy to promote electrons from the valence to the conduction band such that the concentration of electrons affecting the space charge will certainly increase under photon irradiation. Dedicated corrosion experiments separating the effects of neutron and photon irradiations are needed.

Question from Bruce Kammenzind, Bettis Laboratory:—You discussed the role of iron and chromium in relation to Zircaloy-4 but not the role of tin, which has relatively high solubility in Zr and multiple oxidation states. Can you comment on how you see tin affecting conductivity and space charge in the oxide?

Authors' Response:—Tin can be present with 0 charge (metallic state) or as a cation with a +2 or +4 oxidation state in the oxide. If tin is present as a metal or a cation with a +2 charge at a given oxide depth, then it would reduce the amount of space charge at that location; however, if tin is present as a +4 cation then it will have no effect on space charge. That being said, there are very few reports on the oxidation state of tin in Zr oxide. A gradual change in tin oxidation state from 0 to +4 has been reported in Hulme et al. [1], but one cannot rule out the contribution from the metal in the XANES signal due to the experimental setup configuration adopted in that study. On the other hand, according to the C4 model, if all of the tin in Zircaloy-4 is in solid solution with an oxidation state below +4, then there would be enough tin to compensate all space charges in the oxide and the oxidation kinetics would be parabolic. The fact that Zircaloy-4 oxidation kinetics are clearly sub-parabolic contradicts that hypothesis, such that it is likely that most of the tin has a +4 oxidation state. Clear experimental evidence is needed to draw a conclusion on that specific point.

[1] Hulme, H., Baxtera, F., Babua, P., Deneckeb, M. A., Gassc, M., Steuwerd, A., Noréne, K., Carlsone, S., and Preuss, M., “An X-Ray Absorption Near-Edge Structure (XANES) Study of the Sn L_3 Edge in Zirconium Alloy Oxide Films Formed during Autoclave Corrosion,” *Corr. Sci.*, Vol. 105, April 2016, pp. 202–208.

Questions from Brent Heuser, University of Illinois:

1. The cubic kinetics you measured had $n = 0.27$ with a 10 % space charge, whereas your model gives $n = 0.37$. Is this difference important?
2. The oxide microstructure (grain size, morphology) is a function of oxide depth. Grain boundary diffusion of oxygen (and hydrogen) could therefore vary with depth. Will this not affect the barrier height and the space-charge effect?

Authors’ Response:

1. The measured cubic kinetics gives $n = 0.27$ after 90 days of exposure (2 µm oxide thickness). The model gives $n = 0.37$ for a 10 % space charge in the oxide for a very thin oxide (200 nm oxide thickness). Thus, a direct comparison between the two is not possible at the moment. However, the model directly shows that an increase in oxide space charge results in sub-parabolic kinetics. To compare the n values between experiments and theory, we are currently working on modeling longer exposure times (thicker oxides).
2. If a parameter playing a role on charged species transport is time-dependent (or varies with oxide depth, as long as this variation is not linearly dependent on time), then it would affect the corrosion kinetics exponent n. If one focuses on diffusion pathways, it is generally accepted that thicker oxides are more porous than thin ones. Consequently, if diffusion under a concentration gradient is driving the transport of species through the oxide, the oxidation kinetics should be super-parabolic (n greater than 0.5), which is not observed experimentally. Sub-parabolic kinetics implies that the barrier height for transport of charged species across the oxide increases with exposure time. The naturally occurring space-charge build-up in the oxide results in an increase in barrier height and is believed to be the reasons for the sub-parabolic kinetics observed for some Zr alloys.

Question from Hans-Olof Andrén, Chalmers University of Technology:—Your theory basically regards the oxide layer as a homogeneous bulk. How does microstructure affect transport in the oxide—grain boundaries, second-phase particles, etc.?

Authors’ Response:—We recognize that the complex oxide microstructure is not modeled in this theory. One of our future objectives is to include more microstructure effect in the C4 model, e.g., by taking into account the precipitate effect on charged species transport.

Question from Paul Cantonwine, Global Nuclear Fuel:—It is well known that Zircaloy-2 has increased hydrogen pickup compared with Zircaloy-4. This difference has always been linked to nickel in Zircaloy-2. What is your explanation of this difference in hydrogen pickup performance?

Authors' Response:—Indeed, the increase in hydrogen pickup of Zircaloy-2 has been ascribed to an effect of nickel. The general theory is that for hydrogen to be picked up in the oxide and diffuse, it needs a driving force (provided by the electric field, which is highly dependent on the oxide bulk space charges) and a point of entry (where the barrier height for absorption would be lower than in most other locations in the oxide). We believe that nickel at the oxide surface may provide an easy entry point such that for a given driving force it may be easier for a proton to be absorbed in the oxide when nickel is present.

Question from Philippe Bossis, CEA:—Can the proposed model predict the kinetics of oxidation and hydriding of Zr-1Nb alloy annealed at low temperature as presented in Hu et al. [2]?

Authors' Response:—The Zr-1Nb alloy annealed at low temperature presents a complex microstructure with both niobium in solid solution and β-niobium precipitates, such that the oxide layer is heterogeneous in nature. The C4 model has not been applied for heterogeneous precipitate-forming alloys because the oxide layer conductivity is not straightforward to calculate in that case. We are currently trying to resolve that gap.

[2] Hu, J., Setiadinata, B., Aarholt, T., Garner, A., Vilalta-Clemente, A., Partezana, J., Frankel, P., Bagot, P., Lozano-Perez, S., Wilkinson, A., Preuss, M., Moody, M., and Grovenor, C., "Understanding Corrosion and Hydrogen Pickup of Zirconium Fuel Cladding Alloys: The Role of Oxide Microstructure, Porosity, Suboxide, and Second-Phase Particles," *Zirconium in the Nuclear Industry: 18th International Symposium, ASTM STP1597*, R. J. Comstock and A. T. Motta, Eds., ASTM International, West Conshohocken, PA, 2018, pp. 93–126.

Question from Ian MacLaren, University of Glasgow:—How do you intend to quantitatively measure niobium oxidation states?

Authors' Response:—We have measured quantitatively the niobium oxidation states using XANES at the APS synchrotron as detailed herein and in Couet et al. [3].

[3] Couet, A., Motta, A. T., de Gabory, B., and Cai, Z., "Microbeam X-Ray Absorption Near-Edge Spectroscopy Study of the Oxidation of Fe and Nb in Zirconium Alloy Oxide Layers," *J. Nucl. Mater.*, Vol. 452, Nos. 1–3, 2014, pp. 614–627.

Question from Chris Grovenor, University of Oxford:—The Nuclear Power Institute of China reports good corrosion performance in a Zr-1Sn-1Nb-0.3Fe alloy. Do you think that the higher iron content than normal is contributing in your space-charge model to the improved properties by providing some additional Fe^{2+}/Fe^{3+} ions than are available in the lower iron alloys?

Authors' Response:—If the alloy composition is at thermodynamic equilibrium, then any increase in iron content would increase the volume fraction of precipitates because the iron concentration is solid solution is already saturated. Thus, as far as the iron in solid solution is concerned, the C4 model predicts no improvement in corrosion performance by increasing the iron content from 0.1 to 0.3 wt.%. However, the C4 model has not been applied for heterogeneous precipitate-forming alloys because the oxide layer conductivity is not straightforward to calculate in that case. Thus, we cannot yet conclude how an increase in precipitate volume fraction affects corrosion.

Question from Stanislav Linhart, ALVEL, a.s.:—You have shown some data with corrosion kinetics. You observed that there is a "change" or "break" in corrosion kinetics for the Zr-1Nb alloy at an exposure time of approximately 70 days. According to experience and the literature, this change occurs at an exposure of approximately 200 days. Can you please explain the difference?

Authors' Response:—This change in oxidation kinetics (called oxide transition) in Zr-1.0Nb annealed at high temperatures happens after 75 days of autoclave exposure at 360°C. The high-temperature annealing step changes the alloy microstructure. Consequently, the oxidation kinetics are different compared with a low-temperature annealed Zr-1.0Nb alloy, which is the alloy mentioned in the question.